

AD-A099 181

GEORGIA INST OF TECH ATLANTA
PARAMETRIC INVESTIGATION OF RADOME ANALYSIS METHODS. VOLUME I. --ETC(U)
FEB 81 G K HUDDLESTON, H L BASSETT

F/8 17/9
--ETC(U)

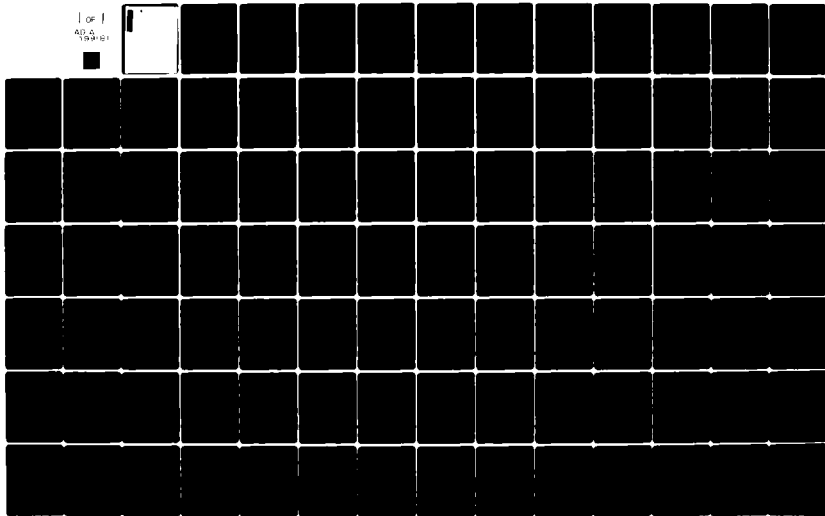
AFOSR-77-3469

NL

UNCLASSIFIED

AFOSR-TR-81-0459

[OF]
AD-A
199181



AD A099181

UNCLASSIFIED

SECURITY CLASSIFICATION OF THIS PAGE (When Data Entered)

18 REPORT DOCUMENTATION PAGE		READ INSTRUCTIONS BEFORE COMPLETING FORM	
1. REPORT NUMBER AFOSR-TR-81-0459	2. GOVT ACCESSION NO. AD-A099	3. RECIPIENT'S CATALOG NUMBER 282	
4. TITLE (and Subtitle) PARAMETRIC INVESTIGATION OF RADOME ANALYSIS METHODS, SALIENT RESULTS. Volume I.		5. TYPE OF REPORT & PERIOD COVERED Final Technical Report, Vol. 1 of 4, 30 Sept. '77- 31 Dec. '80	
6. AUTHOR G. K. Huddleston, H. L. Bassett, & J. M. Newton		7. PERFORMING ORG. REPORT NUMBER AFOSR-77-3469	
8. PERFORMING ORGANIZATION NAME AND ADDRESS Georgia Institute of Technology School of Electrical Engineering & Engineering Experiment Station, Atlanta, GA 30332		9. PROGRAM ELEMENT, PROJECT, TASK AREA & WORK UNIT NUMBERS 61102F 16 17 2301/A6	
10. CONTROLLING OFFICE NAME AND ADDRESS Air Force Office of Scientific Research/NP Physics Directorate Bolling Air Force Base, D. C. 20332		11. REPORT DATE February 1981	
12. MONITORING AGENCY NAME & ADDRESS (if different from Controlling Office)		13. NUMBER OF PAGES 92	
14. DISTRIBUTION STATEMENT (of this Report) Approved for public release; distribution unlimited.		15. SECURITY CLASS. (of this report) UNCLASSIFIED	
17. DISTRIBUTION STATEMENT (of the abstract entered in Block 20, if different from Report)		15a. DECLASSIFICATION/DOWNGRADING SCHEDULE	
18. SUPPLEMENTARY NOTES			
19. KEY WORDS (Continue on reverse side if necessary and identify by block number) Radome Analysis Electromagnetic Analysis Boresight Error			
20. ABSTRACT (Continue on reverse side if necessary and identify by block number) The salient results, conclusions, and recommendations are presented for a three-year program of research to assess the accuracies and ranges of vali- dities of computer-aided methods of radome analysis.			

DD FORM 1 JAN 73 1473

UNCLASSIFIED
SECURITY CLASSIFICATION OF THIS PAGE (When Data Entered)

PARAMETRIC INVESTIGATION OF RADOME ANALYSIS METHODS:

SALIENT RESULTS

by

G. K. Huddleston, H. L. Bassett, & J. M. Newton
School of Electrical Engineering &
Engineering Experiment Station
Georgia Institute of Technology
Atlanta, Georgia 30332

Final Technical Report, Volume I of IV

for

Air Force Office of Scientific Research (AFSC)
Physics Directorate (Code NP-77-148)
Bolling Air Force Base, D. C. 20332

under

Grant AFOSR-77-3469
30 September 1977 - 31 December 1980

February 1981

AIR FORCE OFFICE OF SCIENTIFIC RESEARCH (AFSC)
NOTICE OF TRANSMITTAL TO DDC
This technical report has been reviewed and is
approved for public release IAW AFR 190-12 (7b).
Distribution is unlimited.
A. D. BLOSE
Technical Information Officer

Table of Contents

<u>Section</u>	<u>Page</u>
I. Introduction	
II. Results.	
III. Conclusions and Recommendations.	
Appendix A	
Appendix B	
Appendix C	

Accession For	
NTIS GRA&I	<input checked="" type="checkbox"/>
DTIC TAB	<input type="checkbox"/>
Unannounced	<input type="checkbox"/>
Justification	<input type="checkbox"/>
By	
Distribution/	
Availability	
Dist	
A	

PARAMETRIC INVESTIGATION OF RADOME

ANALYSIS METHODS: SALIENT RESULTS

I. Introduction

The final technical report on this three-year radome research program consists of four volumes. This report, Volume I, presents the salient results, conclusions, and recommendations of this research whose objective was to develop a general theory of radome analysis and to determine the accuracies and ranges of validity of three particular computer-aided radome analysis methods. The results are presented in appendices as copies of papers prepared for publication as summarized in the main body of this report.

Volume II documents the analytical method and Fortran computer code used to analyze the antenna/radome combinations using a fast receiving formulation based on Lorentz reciprocity and geometrical optics. Volume III documents the analytical method and additional Fortran software required for radome analysis based on the Huygens-Fresnel principle or surface integration. Volume IV documents the pattern and boresight error measurements made on eight combinations of three monopulse antennas and five tangent ogive radomes at 35 GHz.

Measured data is used as true data in assessing the accuracies of the computer codes. It is expected that the measured data obtained will be used in the future for similar purposes. It is also expected that the documented computer codes will serve as part of a technology base for use by researchers and practitioners in the radome technical community.

II. Results

Appendix A presents a paper which describes the theory of radome analysis developed during this investigation. The theory is simply an application

of the Huygens-Fresnel principle and Lorentz reciprocity to the radome problem. All methods of radome analysis appearing in the literature are embodied in this general theory. It provides the correct framework in which to think about radome analysis and to make objective comparisons between the various methods of analysis.

Appendix B presents a paper describing some antenna synthesis work that was undertaken during this research. A procedure is described whereby the aperture fields of the four-horn monopulse antenna without radome can be synthesized from measured, amplitude-only, far-field, principal plane patterns. A priori information about the geometry and excitation of the actual antenna is used to find a credible solution to an inverse source problem for which there would otherwise be no unique solution. In the absence of the radome, each analysis method accurately predicts the measured patterns.

Appendix C presents comparisons of measured and computed boresight errors and radome losses for four of the eight antenna/radome combinations considered. The antennas and radomes used are briefly described. (More detailed descriptions are presented in Volume IV.) Qualitative conclusions about the accuracies of the methods can be made from the data presented; in addition, recommendations for future work are brought to light.

III. Conclusions and Recommendations

From the data presented in Appendix C, it is concluded that none of the computer aided radome analysis methods investigated consistently and accurately predicted the boresight errors and losses of the various antenna/radome combinations used. For moderate size antennas and radomes (as defined in Appendix C), the fast receiving method predicts boresight errors reasonably accurately and is perhaps the fastest method available anywhere; however, for

small radomes and large radomes, the accuracy of the error predictions is not as good.

The surface integration method was not completely assessed for predictive accuracy because of unresolved problems with the code. A large part of the problem with the development of the code was the relatively long execution times required on the Cyber 70 system used. It is clear that because of the long execution times, use of the surface integration method will be restricted to the analysis of small radomes.

It is recommended that some "fine tuning" be done on the fast receiving method to improve its predictive accuracy over a larger range of antenna/radome parameters. Specifically, the ray tracing procedure should be modified to account for refractive effects and propagation of the fields along the rays. The expected improvement in accuracy, coupled with the inherent practicality of this code, make this recommended endeavor worthwhile.

It is also recommended that work be continued on the development of the surface integration method of analysis so that its predictive accuracy can be clearly established. A dedicated, small computer system (32-bit word length) is recommended for this work to avoid the anticipated high costs associated with very heavy use of a time-share system such as the Cyber 70 at Georgia Institute of Technology.

It is recommended that exact solutions of carefully selected antenna/radome configurations be obtained for use as true data in the assessment of the accuracies of various computer-aided radome analysis methods. Configurations used must conform to those expected in the applications. The accuracies of the solutions and the solutions themselves must be impeccable. Until such time as this recommendation is carried out, measured data must continue to be used as true data.

As a parallel approach to exact solutions, it is recommended that numerical solutions be obtained on practical configurations of interest using modern numerical methods such as method of moments and integral equation formulations. The use of specialized computing structures for dedicated application to such electromagnetic radiation and scattering problems should be investigated.

Finally, it is recommended that experimental techniques be developed to help isolate deficiencies in the methods of analysis. The usual measurements of patterns and boresight errors simply do not provide the necessary information to pinpoint invalid assumptions and poor approximations in any analysis procedure. New experimental methods which make use of automated measurements and near-field/far-field transformations need to be developed.

APPENDIX A

"Theory of Radome Analysis"

Submitted for Review for Publication

in

IEEE Transactions of the Antennas and Propagation Society

November 1980

THEORY OF RADOME ANALYSIS

G. K. Huddleston
School of Electrical Engineering
Georgia Institute of Technology
Atlanta, Georgia 30332

Abstract

A basic theory of radome analysis is presented based on the reciprocity theorem and the Huygens-Fresnel principle. Receiving and transmitting formulations are developed. Techniques of analysis are presented to distinguish the salient features of radome analysis and to show the relationships between the theory and some existing methods of analysis. The equivalence between the receiving and transmitting cases is also established, both in general and explicitly for the far-field case.

I. INTRODUCTION

Radome analysis is the application of electromagnetic theory to determine the effects of protective dielectric structures on the electrical characteristics of antennas enclosed by them. Numerous methods of analysis have been developed for the prediction of radome effects; however, no unified theory has been advanced to provide a common basis of understanding of the various approaches taken and the approximations used therein. Furthermore, no comprehensive measurements have been reported which provide true data in determining the accuracies of the various methods when parameters such as antenna size, wavelength, radome size and shape are considered over the ranges that they are likely to assume in the applications.

This paper presents a theory of radome analysis which embodies known methods of analysis that have appeared in the literature. The theory is based on the reciprocity theorem [1] and the Huygens-Fresnel principle for electromagnetic fields [2,3] both of which are derivable from Maxwell's equations via the divergence theorem and the vector Green's theorem. The reciprocity theorem serves as the basis for the receiving formulation of radome analysis, and the Huygens-Fresnel principle is the basis for the transmitting formulation as seen in what follows. The equivalences of the two formulations are also established. Some approximations and techniques used in implementing the analyses are presented along with discussions which clarify the justifications for the approaches used in practice.

The development and presentation of this theory of radome analysis is motivated by an on-going parametric investigation of radome analysis methods [4]. Measured pattern data and boresight error data for three antenna sizes combined in fifteen combinations with five radomes have been obtained to serve as true data in determining the accuracies and ranges of validities of three common computer-aided analyses. Great care has been taken to ensure accurate modeling of the antennas such that, in the absence of a radome, each computer code accurately predicts the measured radiation patterns [5]. The theory provides the framework in which the methods can be compared, especially in regard to the approximations used, the validity of various assumptions made, and the equivalence of different computational procedures which yield, or should yield, the same result. The theory also provides the basis for developing test cases to verify the computer codes.

Development of radome analysis methods have paralleled the development of airborne radar systems whose complexities have increased over the years. Silver [6] illustrates the geometrical optics approaches taken up to 1949 and which were developed during the previous war years. Kilcoyne [7] presented a two-dimensional ray tracing method for analyzing radomes which utilized the digital computer, and is an extension of work done earlier by Snow [8] and by Pressel [9]. A more rigorous method of analysis was introduced in the same year by Van Doeren [10] using an integral equation to compute fields inside the radome caused by an incident plane wave. Tricoles [11] formulated a three-dimensional method of radome analysis based on Shelkunoff's induction and equivalence theorems. Tavis [12] describes a three-dimensional ray tracing technique to find the fields on an equivalent aperture external to an axially symmetric radome.

Paris [13] describes a three-dimensional radome analysis wherein the tangential fields on the outside surface of the radome due to the horn antenna radiating inside the radome are found. Wu and Rudduck [14] describe a three-dimensional method which uses the plane wave spectrum representation to characterize the antenna. Joy and Huddleston [15] describe a computationally fast, three-dimensional radome analysis which utilizes the plane wave spectrum (PWS) representation and exploits the Fast Fourier Transform (FFT) to speed up the computer calculations. Chesnut [16] has combined the program of Wu and Rudduck with the work of Paris to form a three-dimensional radome analysis method. Huddleston [17] has recently developed a three-dimensional radome analysis method which uses a general formulation based on the Lorentz reciprocity theorem. Siwiak, et al., [18] have recently applied the reaction theorem to the analysis of a tangent ogive radome at X-band frequencies to determine boresight error. Hayward, et al., [19] have compared the accuracies of two methods of analysis in the cases of large and small radomes to show that ray tracing does not accurately predict wavefront distortion in the case of small radomes.

II. RECEIVING FORMULATION

The reciprocity theorem is a starting point for the formulation of a unified theory of radome analysis. The general reciprocity theorem [1] states that

$$\oint_S (\underline{E}_a \times \underline{H}_b - \underline{E}_b \times \underline{H}_a) \cdot \hat{n} \, da = \int_V (\underline{E}_b \cdot \underline{J}_a - \underline{E}_a \cdot \underline{J}_b - \underline{H}_b \cdot \underline{J}_a^m + \underline{H}_a \cdot \underline{J}_b^m) \cdot dV \quad (1)$$

where the surface S encloses the volume V containing two sets of electric and magnetic sources $(\underline{J}_a, \underline{J}_a^m), (\underline{J}_b, \underline{J}_b^m)$ which give rise to electromagnetic fields $(\underline{E}_a, \underline{H}_a), (\underline{E}_b, \underline{H}_b)$, respectively. (Time variations of the form $e^{j\omega t}$ are understood and suppressed).

Figure 1 illustrates a typical radome analysis situation where it is desired to determine the response V_a of Antenna "a" to fields produced by Antenna "b". The closed surface S in the reciprocity theorem is chosen to be $S_0 + S_1$ so that the volume V is the source-free region lying between Antenna "a" and the inner surface of the dielectric enclosure depicted in Figure 1. In this case, the right side of Equation (1) equates to zero (Lorentz reciprocity theorem), and the left side can be separated into two surface integrals as

$$-\int_{S_0} (\underline{E}_a \times \underline{H}_b - \underline{E}_b \times \underline{H}_a) \cdot \hat{n} \, da = \int_{S_1} (\underline{E}_a \times \underline{H}_b - \underline{E}_b \times \underline{H}_a) \cdot \hat{n} \, da \quad (2)$$

where \hat{n} is the unit normal to the surface and is directed positively out of the volume V . The fields $\underline{E}_a, \underline{H}_a$ are those produced on S_1 and S_0 by Antenna "a" when it is activated (transmitting); $\underline{E}_b, \underline{H}_b$ are the fields produced on S_1 and S_0 when Antenna "b" is activated (and Antenna "a" is passive or receiving).

Let surface S_0 be divided into two parts: S_0' consisting of that portion of S_0 across the waveguiding structure connecting the generator of Antenna "a" to the radiating structure; S_0'' consisting of the remainder of S_0 and which coincides with the conducting surface of the antenna as indicated in the figure. The integral of the fields over S_0'' is identically zero [20] so that the left side of Equation (2) reduces to the integration over S_0' . Now, in the many practical cases of interest, there exists a dominant mode of propagation over S_0' (e.g., TE_{10}

SOURCE b

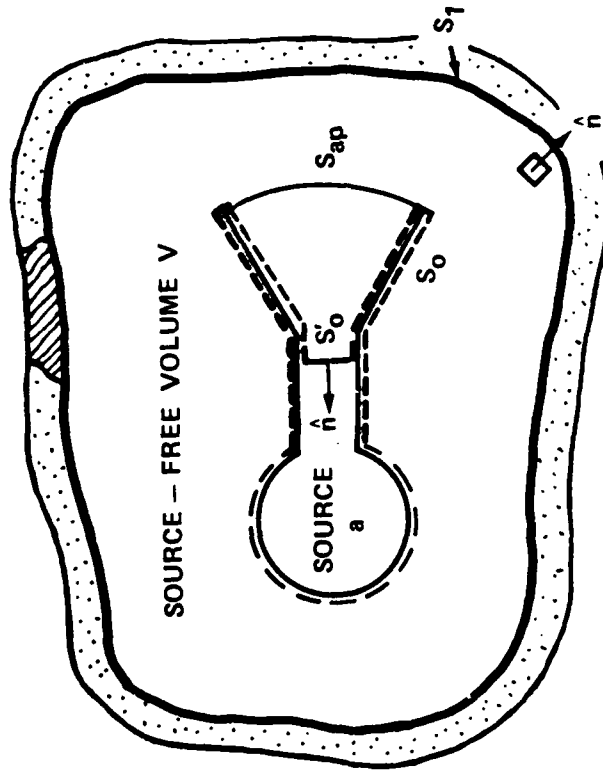


FIGURE 1. GEOMETRY FOR RECEIVING FORMULATION USING RECIPROCITY THEOREM.

mode in rectangular waveguide) so that currents and voltages can be defined at this terminal plane so that there results

$$V_a I_b + V_b I_a = - \int_{S_0} (\underline{E}_a \times \underline{H}_b - \underline{E}_b \times \underline{H}_a) \cdot \hat{n} da \quad (3)$$

The currents and voltages are defined for the two cases of interest in Figure 2:

V_a, I_a - Voltage and current produced at S_0' by generator "a" when generator "b" is passive;

V_b, I_b - Voltage and current produced at S_0' by generator "b" when generator "a" is passive.

Linear impedance relationships can also be defined as indicated in Figure 2 such that (using $Y = 1/Z$)

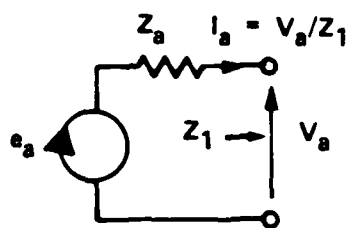
$$V_a I_b + V_b I_a = V_a (V_b Y_a) + V_b (V_a Y_1) \quad (4)$$

Equating Equation (4) to Equation (2) and solving for the received voltage V_b results in

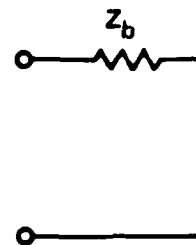
$$V_b = \frac{V_{REC}}{V_a (Y_a + Y_1)} = \frac{1}{V_a (Y_a + Y_1)} \int_{S_1} (\underline{E}_a \times \underline{H}_b - \underline{E}_b \times \underline{H}_a) \cdot \hat{n} da \quad (5)$$

where V_{REC} has been defined for convenience. This is one desired result.

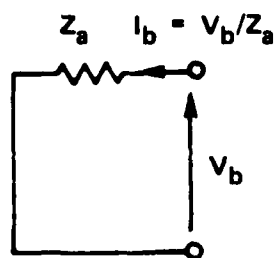
In most analysis situations, Antenna "a" and the dielectric enclosure comprise the antenna/radome combination. The separation of this combination and Antenna "b" can be made very large so that the fields of "b" are those of a transverse electromagnetic plane wave incident on the radome. In radar applications, the distant target is illuminated either



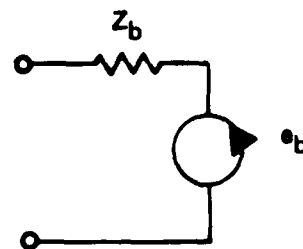
(a) Source "a" active,



Source "b" passive



(b) Source "a" passive,



Source "b" active

FIGURE 2. DEFINITIONS OF CIRCUIT PARAMETERS OF THE ANTENNAS.

by Antenna "a" or another antenna not shown in Figure 1. The reflection from the target comprises Antenna "b" in the analysis and, for large separation, arrives, again, as an incident plane wave on the radome. Note, however, that the receiving formulation embodied in Equation (5) is valid for either the near-field (small separation) or far-field (large) case. Also, superposition applies so that multiple targets or sources can be accommodated as linear combinations comprising the fields $\underline{E}_b, \underline{H}_b$ in Equation (5).

Equation (5) is exact; however, in the evaluation of the integral, approximations to the actual fields on S_1 may be introduced so that inaccuracies in the computation of the received voltage may result. To see the effects of certain approximations, it is advantageous to make the following definitions of primary and scattered fields:

$$\underline{E}_a = \underline{E}_{ao}^i + \underline{E}_{as} + \underline{E}_{as}' \quad (6)$$

$$\underline{H}_a = \underline{H}_{ao}^i + \underline{H}_{as} + \underline{H}_{as}' \quad (7)$$

where

- $\underline{E}_{ao}^i, \underline{H}_{ao}^i$ - Fields on S_1 due to Antenna "a" which contain no scattered field components; i.e., the fields that would exist on S_1 in the absence of the dielectric.
- $\underline{E}_{as}, \underline{H}_{as}$ - First order scattered fields on S_1 due to Antenna "a"; i.e., fields reflected only once from material media outside S_1 and from Antenna "b".
- $\underline{E}_{as}', \underline{H}_{as}'$ - Higher order scattered fields on S_1 due to Antenna "a"; i.e., components caused by multiple scattering

between Antenna "a" and surrounding media, including Antenna "b".

Similar definitions can be made for Antenna "b" with respect to the surface S_1 as follows:

$$\underline{E}_b = \underline{E}_{bo}^t + \underline{E}_{bs} + \underline{E}_{bs}' \quad (8)$$

$$\underline{H}_b = \underline{H}_{bo}^t + \underline{H}_{bs} + \underline{H}_{bs}' \quad (9)$$

where \underline{E}_{bo}^t , \underline{H}_{bo}^t are the fields on S_1 due to Antenna "b" and which contain no scattered components due to material media inside S_1 , including Antenna "a". The fields \underline{E}_{bs} , \underline{H}_{bs} are first order scattered fields on S_1 due to a single scattering from Antenna "a". The fields \underline{E}_{bs}' , \underline{H}_{bs}' are the higher order scattered fields. When these definitions are substituted into Equation (5) and the vector cross products evaluated, there results

$$\begin{aligned} V_{\text{REC}} = & \int_{S_1} (\underline{E}_{ao}^i \times \underline{H}_{bo}^t - \underline{E}_{bo}^t \times \underline{H}_{ao}^i) \cdot \hat{n} \, da \\ & + \int_{S_1} (\underline{E}_{ao}^i \times \underline{H}_{bs} - \underline{E}_{bs} \times \underline{H}_{ao}^i) \cdot \hat{n} \, da \\ & + \int_{S_1} (\underline{E}_{as} \times \underline{H}_{bo}^t - \underline{E}_{bo}^t \times \underline{H}_{as}) \cdot \hat{n} \, da \\ & + \int_{S_1} (\underline{E}_{as} \times \underline{H}_{bs} - \underline{E}_{bs} \times \underline{H}_{as}) \cdot \hat{n} \, da \\ & + \text{Terms involving higher order scattered fields} \quad (10) \end{aligned}$$

The first integral on the right side of Equation (10) provides the primary contribution to the received voltage for those cases of interest where the dielectric is somewhat transparent to the incident fields $\underline{E}_{bo}^i, \underline{H}_{bo}^i$ of Antenna "b". The second and third integrals are each identically zero by virtue of the definitions of the scattered fields and the general reciprocity theorem as applied to the source-free volume \bar{V} consisting of the region outside S_1 ; i.e., since there are no sources of the defined fields in this region, the right side of Equation (1) and, hence, the second integral of Equation (10), are both zero. A similar argument holds for the third integral when the general reciprocity theorem is applied to the source-free region V enclosed by S_1 .

The contribution of the fourth integral in Equation (10) depends on the scattering properties of Antenna "a" as well as on the reflective properties of the dielectric enclosure with respect to the incident fields $\underline{E}_{ao}^i, \underline{H}_{ao}^i$. It is difficult to assess the significance of these contributions and those of the integrals involving higher order scattered fields. At any rate, it is impractical in current computer-aided analyses to include scattering from the antenna inside the enclosure; hence, only the first term in Equation (10) is usually retained. The objective of practical radome analysis then centers on the determination of the fields in the integral

$$V_{REC} \approx \int_{S_1} (\underline{E}_{ao}^i \times \underline{H}_{bo}^t - \underline{E}_{bo}^t \times \underline{H}_{ao}^i) \cdot \hat{n} \, da \quad (11)$$

and on the evaluation of the integral itself.

Surfaces other than the inside surface S_1 of the dielectric of Figure 1 can also be selected for the evaluation of the received voltage

via Equation (10) or (11). For example, choose S_0 as before and choose S_1 to also coincide with the outer surface of Antenna "a", including the radiating aperture portion S_{ap} . Apply Lorentz reciprocity to the source-free volume contained between the antenna aperture and S_0' to yield

$$V_{REC} \approx \int_{S_{ap}} (\underline{E}_{ao}^i \times \underline{H}_{bo}^t - \underline{E}_{bo}^t \times \underline{H}_{ao}^i) \cdot \hat{n} \, da \quad (12)$$

The fields $\underline{E}_{ao}^i, \underline{H}_{ao}^i$ are the aperture fields of Antenna "a" when it is transmitting in the absence of the dielectric and are often known or specified for analysis purposes. The real difficulty arises in the determination of the fields $\underline{E}_{bo}^t, \underline{H}_{bo}^t$ on the chosen surface S_1 . And it is the choice of the surface S_1 and the approximations used to find the fields on it which distinguish the various methods of analysis based on the receiving formulation. More will be said concerning the determination of these fields in the next section.

Another choice of the surface of integration consists of the outer surface S_3 of the dielectric enclosure of Figure 1. First apply Equation (1) to the source-free region consisting of the dielectric itself as enclosed by its inner surface S_1 and its outer surface S_3 ; i.e., $S = S_1 + S_3$. Since the right side of Equation (1) is zero, and since the positive direction of \hat{n} is out of V , it is seen from Equation (5) that

$$V_{REC} = \int_{S_3} (\underline{E}_a \times \underline{H}_b - \underline{E}_b \times \underline{H}_a) \cdot \hat{n} \, da \quad (13)$$

where \hat{n} is the unit outward normal to the outer surface of the dielectric. It will be shown in a later section that Equation (13) is equivalent to the transmitting formulation to be discussed next.

III. TRANSMITTING FORMULATION

A second generalized approach to radome analysis uses a transmitting formulation which does not explicitly consider the fields produced by the incident fields of a source outside the dielectric structure. Instead, the equivalence and uniqueness theorems of electromagnetics [21] are invoked to establish the result that the fields radiated by Antenna "a" into the unbounded, homogeneous region outside the dielectric enclosure can be found from knowledge of the tangential electric and magnetic fields on the outer surface of the dielectric. Moreover, there exists an integral formula for the actual computation of these fields.

After Stratton and Chu [2], Silver [3] derives the general solution for the time-harmonic electromagnetic fields in a homogeneous medium which arise from a prescribed set of sources, including magnetic (equivalent) charges and currents. The derivation is based on Maxwell's equations (including the equations of continuity for charges and currents), a vector Green's theorem, and the free-space Green's function $\psi = e^{-jk_r r}$. The results, Equations (3.108) and (3.109) of Silver, are called the Huygens-Fresnel principle (also called Kirchhoff-Huygens principle) and are repeated here for convenience:

$$\underline{E}(x', y', z') = + \frac{T}{4\pi} \int_S [-j\omega\mu\psi(\hat{n} \times \underline{E}) + (\hat{n} \times \underline{E}) \times \nabla\psi + (\hat{n} \cdot \underline{E}) \nabla\psi] dS \quad (14)$$

$$\underline{H}(x', y', z') = \frac{T}{4\pi} \int_S [j\omega\epsilon(\hat{n} \times \underline{E})\psi + (\hat{n} \times \underline{H}) \times \nabla\psi + (\hat{n} \cdot \underline{H}) \nabla\psi] dS \quad (15)$$

where \hat{n} is the unit normal to S which points into the source-free medium as indicated in Figure 3.

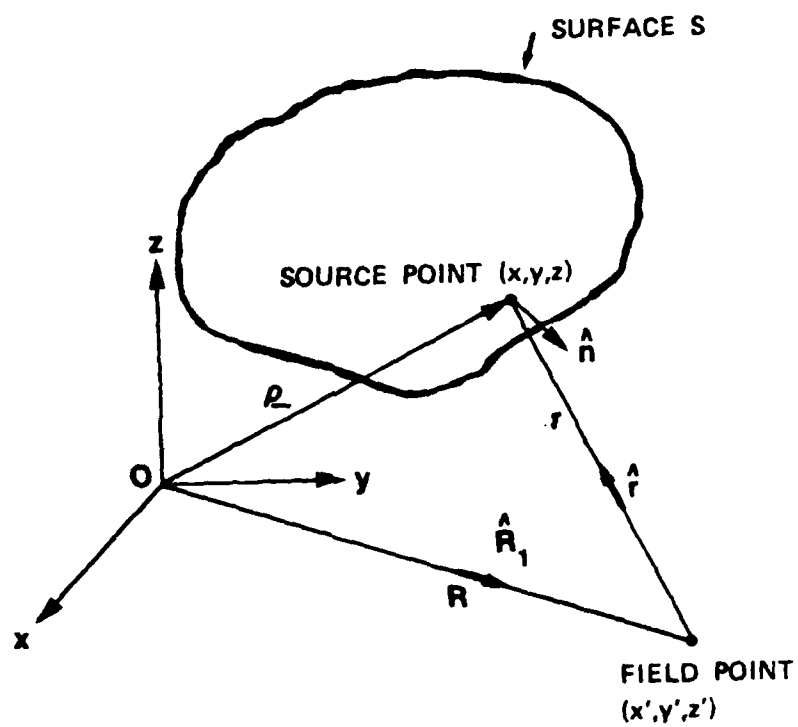


FIGURE 3. GEOMETRY FOR HUYGENS-FRESNEL PRINCIPLE.

In the above equations, primed variables are the coordinates of the point at which the field is to be computed, and unprimed coordinates are used to designate the source coordinates lying on the surface S. The distance r is measured from the field point (x', y', z') to the source point (x, y, z) so that

$$r = \sqrt{(x-x')^2 + (y-y')^2 + (z-z')^2} \quad (16)$$

and

$$\nabla\psi = - (jk + \frac{1}{r})\psi \hat{r} = (jk + \frac{1}{r})\psi \hat{r}_1 \quad (17)$$

where $\hat{r} = -\hat{r}_1$ is a unit vector directed along r from the field point to the source point. The variable T is adopted from the notation of Poggio and Miller [22] so that the fields at points on S can also be included; it is given by

$$T = \frac{1}{1-\Omega/4\pi} = \begin{cases} 1 & \text{if } \Omega=0, (x', y', z') \text{ not on } S \\ 2 & \text{if } \Omega=2\pi, (x', y', z') \text{ on } S \end{cases} \quad (18)$$

The terms $(\hat{n} \times \underline{E})$, $(\hat{n} \times \underline{H})$ in Equations (14) and (15) can be considered as equivalent magnetic and electric surface current densities

$$\underline{K} = \hat{n} \times \underline{H} \quad (19)$$

$$\underline{K}_m = - (\hat{n} \times \underline{E}) \quad (20)$$

with corresponding equivalent surface charge densities

$$\eta = (\hat{n} \cdot \underline{E}) \quad (21)$$

$$\eta_m = (\hat{n} \cdot \underline{H}) \quad (22)$$

These equivalent currents and charges are the sources of the fields \underline{E} , \underline{H} in the region outside the dielectric enclosure. Using the equation of continuity for surface currents and charges [23].

$$\nabla_S \cdot \underline{K} + \frac{\partial \eta}{\partial t} = 0 \quad (23)$$

the terms in Equations (14) and (15) involving normal field components may be rewritten for the time-harmonic case as

$$\hat{n} \cdot \underline{E} = \frac{j}{\omega \epsilon} \nabla_S \cdot (\hat{n} \times \underline{H}) \quad (24)$$

$$\hat{n} \cdot \underline{H} = \frac{j}{\omega \mu} \nabla_S \cdot (\underline{E} \times \hat{n}) \quad (25)$$

where $\nabla_S \cdot$ is the "surface divergence". Thus, the fields \underline{E} , \underline{H} in V are expressible entirely in terms of the tangential fields on S as is in keeping with the uniqueness theorem. (Note, however, that the surface divergence involves first order partial derivatives whose numerical computation may not be desirable.)

Implicit in the application of equivalent surface charges and currents is Love's equivalence principle [24]. It is a special case of the general field equivalence principle [25] in that a null field is postulated inside the surface S , and the charges and currents of Equations (19)-(22)

are required on S to maintain the original field \underline{E} , \underline{H} outside S . Hence, an application of the Huygens-Fresnel integrals using these surface currents to find the fields at a point inside S would necessarily yield a null result. This observation is important when applying the Huygens-Fresnel integrals to find specially defined fields inside the radome as discussed below.

The integral representations in Equations (14) and (15) for the fields radiated by Antenna "a" into the homogeneous, unbounded medium outside the radome are exact for points up to and including the surface S ; however, the difficulty in analysis is the accurate determination of fields \underline{E} , \underline{H} on S . To gain further insight into this problem, consider the geometry of Figure 4. Define primary and scattered fields of the antenna with respect to surfaces S_1 and S_2 as was done in Equations (6) and (7) of the previous section. Let the primary fields \underline{E}_{ao} , \underline{H}_{ao} on S_2 be known. Then the primary fields incident on surface S_1 can be found via Equations (14) and (15) above where the surface of integration is now S_2 of Figure 4; i.e.,

$$\underline{E}_{ao}(S_1) = \frac{1}{4\pi} \int_{S_2} H_F\{\hat{n}, \underline{E}_{ao}, \underline{H}_{ao}\} dS \quad (26)$$

where the Huygens-Fresnel operator $H_F\{ \}$ is defined here to be the integrand of Equation (14). A similar expression holds for the magnetic field intensity \underline{H}_{ao} . By definition, the fields \underline{E}_{ao} , \underline{H}_{ao} are those that would exist at S_1 in the absence of the dielectric.

The first-order scattered fields \underline{E}_{as} , \underline{H}_{as} on S_1 are those caused by the boundary S_1 and the media outside S_1 . A very common approximation for this complicated scattering process utilizes the results

of plane wave interaction with a dielectric interface: at each point on S_1 , the incident fields \underline{E}_{ao} , \underline{H}_{ao} are approximated locally as a plane wave, and the dielectric is assumed to have the same effect as a plane dielectric panel. The normal to the dielectric surface and the direction of propagation of the incident fields define the plane of incidence and the angle of incidence. The incident electric field is resolved into components perpendicular to and parallel to the plane of incidence as illustrated in Figure 5. The flat panel reflection coefficients R_\perp , R_\parallel are then applied to the incident fields to find estimates of the first-order scattered fields; i.e.

$$\underline{E}_{as} \approx \hat{a}_\perp (\underline{E}_{ao} \cdot \hat{a}_\perp) R_\perp + \hat{a}_\parallel (\underline{E}_{ao} \cdot \hat{a}_\parallel) R_\parallel \triangleq \underline{E}_{ao} \cdot \underline{R} \quad (27)$$

where the dyadic \underline{R} is defined.

The flat panel transmission coefficients T_\perp , T_\parallel may also be used to estimate the fields transmitted to the outside surface; i.e.,

$$\underline{E}_{ao}^t \approx \hat{a}_\perp (\underline{E}_{ao} \cdot \hat{a}_\perp) T_\perp + \hat{a}_\parallel (\underline{E}_{ao} \cdot \hat{a}_\parallel) T_\parallel \triangleq \underline{E}_{ao} \cdot \underline{T} \quad (28)$$

$$\underline{H}_{ao}^t = \hat{a}_\perp (\underline{H}_{ao} \cdot \hat{a}_\perp) T_\parallel + \hat{a}_\parallel (\underline{H}_{ao} \cdot \hat{a}_\parallel) T_\perp \triangleq \underline{H}_{ao} \cdot \underline{T}' \quad (29)$$

When \underline{E}_{ao}^t , \underline{H}_{ao}^t are used in Equations (14) and (15), a first-order approximation to the radiated fields outside the dielectric is obtained.

The procedure just described is that used earlier by Paris [13] and emulated by Wu and Rudduck [14] and Chesnut [16]. The direction of propagation \hat{k} of the incident field was taken to be that of the Poynting

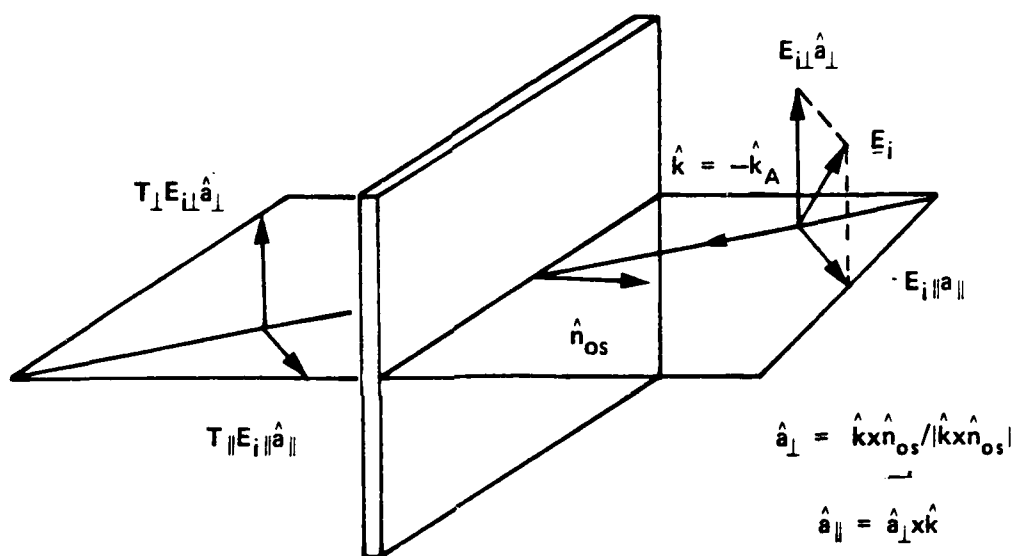


FIGURE 5. PLANE WAVE PROPAGATION THROUGH AN INFINITE PLANE SHEET.

vector or real power flow. Also, since only far-field patterns were of interest, the usual simplifying approximations were applied to Equations (14) and (15) to obtain the following far-field approximations

$$\underline{E}_{ff}(\hat{R}_1) = \frac{-j\omega\mu}{4\pi R} e^{-jkR} \int_{S_3} [\hat{n} \times \underline{H} - ((\hat{n} \times \underline{H}) \cdot \hat{R}_1) \hat{R}_1 + \frac{(\underline{E} \times \hat{n}) \times \hat{R}_1}{\eta_0}] e^{jk \hat{R}_1 \cdot \underline{r}} dv \quad (30)$$

$$\underline{H}_{ff}(\hat{R}_1) = \frac{\hat{R}_1 \times \underline{E}_{ff}}{\eta_0} \quad (31)$$

where $\eta_0 = \sqrt{\mu/\epsilon}$ is the characteristic impedance of free space and where the geometry variables are defined in Figure 4. Note that the second term in the integrand of Equation (30) is the radial component of $\hat{n} \times \underline{H}$ which is subtracted to ensure that only transverse (to \hat{R}_1) components of the fields are found in the far zone. Paris used the fields given by Equations (28) and (29) in the integrand of Equation (30).

The first-order scattered fields \underline{E}_{as} , \underline{H}_{as} on surface S_1 also contribute to the incident fields at the surface S_1 as indicated by the dashed secondary ray in Figure 4. To formulate this contribution, consider the computation of the field \underline{E}_{as} at an interior point P of the volume enclosed by S_1 . Since all sources of \underline{E}_{as} , \underline{H}_{as} are outside S_1 ,

$$\underline{E}_{as}(P) = \frac{T}{4\pi} \int_{S_1} \underline{H}_F \{ -\hat{n}, \underline{E}_{as}, \underline{H}_{as} \} dS \quad (32)$$

where $-\hat{n}$ is the unit inward normal to S_1 and $T=1$. On surface S_1 write \underline{E}_{as} , \underline{H}_{as} as

$$\underline{E}_{as}(S_1) = \underline{E}_{ao} \cdot \underline{R} + \underline{E}_{as}'' \quad (33)$$

$$\underline{H}_{as}(S_1) = \underline{H}_{ao} \cdot \underline{R}' + \underline{H}_{as}'' \quad (34)$$

where \underline{R} , \underline{R}' are flat panel reflection dyadics already defined, and where \underline{E}_{as}'' , \underline{H}_{as}'' represent the contributions to \underline{E}_{as} , \underline{H}_{as} at each point on S_1 from radiation by the fields at every other point. Substitute Equations (33) and (34) into Equation (32) with $T = 2$ for P on S_1 to yield

$$\underline{E}_{as}(S_1) = \frac{1}{2\pi} \int_{S_1} H_F\{-\hat{n}, \underline{E}_{ao} \cdot \underline{R} + \underline{E}_{as}'', \underline{H}_{ao} \cdot \underline{R}' + \underline{H}_{as}''\} dS \quad (35)$$

Carry out the integration on the directly reflected terms to yield

$$\underline{E}_{as}(S_1) = \underline{E}_{ao} \cdot \underline{R} + \frac{1}{2\pi} \int_{S_1'} H_F\{-\hat{n}, \underline{E}_{as}'', \underline{H}_{as}''\} dS \quad (36)$$

where S_1' is surface S_1 with the point of interest excluded.

The fields \underline{E}_{as}'' , \underline{H}_{as}'' are, of course, unknown; however, a first-order approximation to \underline{E}_{as}'' at a point P on S_1 is

$$\underline{E}_{as}''(S_1) \approx \frac{1}{2\pi} \int_{S_1'} H_F\{-\hat{n}, \underline{E}_{ao} \cdot \underline{R}, \underline{H}_{ao} \cdot \underline{R}'\} dS \quad (37)$$

That is, the directly reflected fields at every other point on S_1 are used to determine \underline{E}_{as}'' at the point of interest on S_1 . The fields \underline{E}_{as}' , \underline{H}_{as}' at each point on S_1 should then be added to incident fields \underline{E}_{ao} , \underline{H}_{ao} to produce a second order estimate to the fields on the outside surface of the dielectric via Equations (28) and (29). Hence, an approximate, iterative procedure to compute the effects of the first-order scattered fields on the final radiated fields is formulated.

An important hypothesis for the validity of Equations (14) and (15) is that the fields \underline{E} , \underline{H} on S satisfy Maxwell's equations, including the equations of continuity. If this hypothesis is not met, the fields

computed at points not on S will still satisfy Maxwell's equations provided only that the equations of continuity are satisfied on S ; e.g., if surface currents are terminated abruptly, then a line of surface charge must be explicitly included in the field expressions [26]. If the hypothesis that \underline{E} , \underline{H} on S satisfy Maxwell's equations is met, then the equations of continuity are automatically satisfied; moreover, the expressions in Equations (14) and (15) are valid for points on surface S as well as for points outside. Now, the fields given by Equations (26), (33), (34), and (37) do satisfy Maxwell's equations; however, when the approximation in Equation (37) is substituted into Equation (33), the latter may no longer satisfy Maxwell's equations on S_1 because of the first term. Hence, a number of iterations may be required before the true values of \underline{E}_{as} , \underline{H}_{as} on S_1 are found.

Other approaches to the determination of the first-order scattered fields \underline{E}_{as} , \underline{H}_{as} include the integral equation formulation discussed by Poggio and Miller [22] for scattering from dielectric bodies. In this approach for the geometry of Figure 4, integral expressions are written in each region for the electric and magnetic fields in terms of the equivalent surface currents and charges via Equations (14) and (15). In Region I there are added terms \underline{TE}_{ao} , \underline{TH}_{ao} in the integral expressions due to the incident fields. The boundary conditions at each material interface are then written using the integral expressions, resulting in a system of integral equations in the unknown surface charges and currents. In principle, the equations can be solved by the method of moments [27] or by iterative methods such as discussed above. The radiation fields in Region III could then be found directly from the solutions for the surface currents and charges on S_3 via Equations (14) and (15); however,

the contributions of the higher order scattered fields would not be included.

The techniques discussed in this section for the determination of the fields on a specified surface are directly applicable to the receiving formulation of the previous section. Most notably, in Equation (12), it is necessary to find the fields $\underline{E}_{bo}^t, \underline{H}_{bo}^t$ of Antenna "b" on the surface S_{ap} which coincides with the radiating aperture of Antenna "a". When Antenna "b" is greatly removed, the fields incident on the outside of the dielectric are those of an infinite plane wave. Appropriate adaptations of Equations (28) and (29) could be used to estimate the fields $\underline{E}_{bo}^t, \underline{H}_{bo}^t$ on the inner surface of the dielectric enclosure. The Huygens-Fresnel integrals of Equations (14) and (15) could then be applied to transform these fields to the surface S_{ap} . This approach is essentially that developed by Tricoles [28]. An integral equation approach could also be used, including the one described by Van Doeren [10].

IV. EQUIVALENCE OF FORMULATIONS

It is well known that the receiving and transmitting patterns of an antenna in free space are identical. In this section, it is theoretically demonstrated that the receiving and transmitting patterns for an antenna enclosed by a dielectric radome as in Figure 1 are also identical, and that the receiving and transmitting formulations of radome analysis lead to identical results. Establishment of the equivalence yields insight into the computational advantages of one formulation over the other and provides a means to compare numerical results obtained using the two approaches.

Consider the geometry of Figure 6 where \hat{n}_b represents an infinitesimal electric current source of strength I_b , length Δl , and orientation \hat{n}_b located at the point (x', y', z') which is a great distance R from the origin of coordinates. For definiteness, \hat{n}_b is transverse to \hat{R}_1 , which is the orientation that would normally be assigned for the measurement of the radiation pattern of Antenna "a" enclosed by the surface S_3 . The fields \underline{E} , \underline{H} at (x', y', z') due to Antenna "a" are given by Equations (14) and (15). For clarity, let \underline{E}_T , \underline{H}_T represent the fields on S_3 produced by Antenna "a" when it is transmitting.

Let \underline{E}_R , \underline{H}_R be the fields produced on S_3 by the current element \hat{n}_b . An application of the general reciprocity theorem to the unbounded region yields

$$\int_{S_3} (\underline{E}_T \times \underline{H}_R - \underline{E}_R \times \underline{H}_T) \cdot \hat{n} \, dS = - \underline{E} \cdot \hat{n}_b I_b \Delta l \quad (38)$$

A second application of the reciprocity theorem to Antenna "a" inside the surface S_3 as was done in the discussion leading up to Equation (13) yields the result that the complex voltage response of Antenna "a" to the fields \underline{E}_R , \underline{H}_R incident on S_3 is proportional to the integral in Equation (38); hence,

$$V_R = I_b \Delta l \underline{E} \cdot \hat{n}_b = C \int_{S_3} (\underline{E}_T \times \underline{H}_R - \underline{E}_R \times \underline{H}_T) \cdot \hat{n} \, dS \quad (39)$$

where C is a complex constant.

Equation (39) provides the connection between the receiving and transmitting formulations and, as such, represents the third facet of

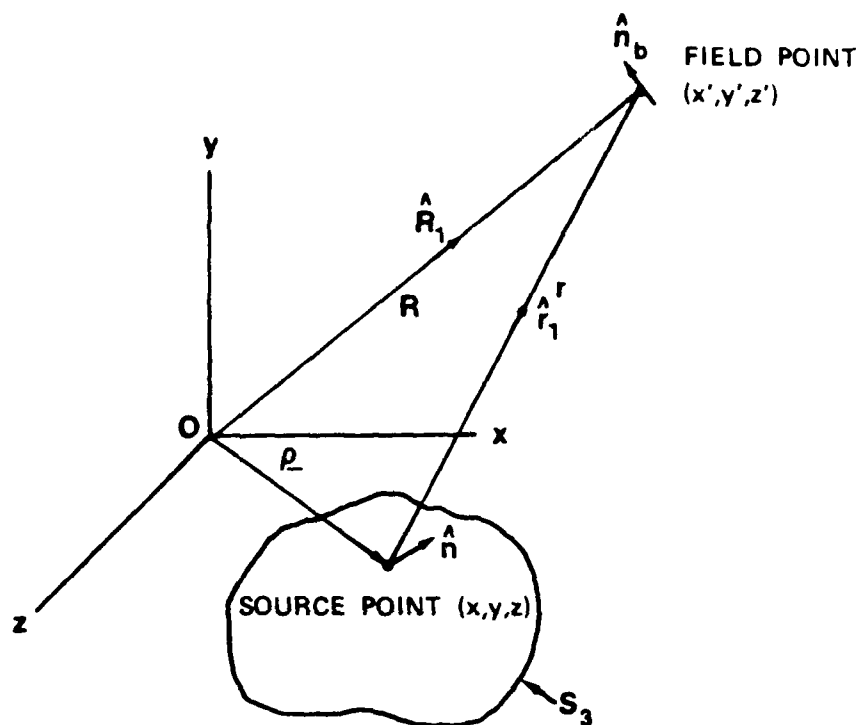


FIGURE 6. GEOMETRY USED TO ESTABLISH EQUIVALENCE BETWEEN THE RECEIVING AND TRANSMITTING FORMULATIONS OF RADOME ANALYSIS.

the theory of radome analysis. Basically, it states that if \underline{E} , \underline{H} are the fields of Antenna "a" at (x', y', z') as determined via the Huygens-Fresnel principle, then the voltage response of Antenna "a" (when receiving) to an elementary current source at (x', y', z') is given succinctly by Equation (39) as $I_b \Delta l \underline{E} \cdot \hat{n}_b$. An antenna more complicated than the elementary current source could be assumed for Antenna "b": for the far-zone case, the same results would be obtained since the radiation and reception properties of the antenna can be embodied in a complex effective vector length \hat{h} which is entirely analogous to \hat{n}_b [29]; for the near-field case, the approach described by Paris et al. [30] would be required.

Even though Equation (39) is valid regardless of the separation and orientation of the elementary source, it is desired here to explicitly establish the second equality in that equation for the far-zone case. To this end, it is noted that the fields \underline{E}_R^i , \underline{H}_R^i on S_3 are those of a plane electromagnetic wave propagating in the $\hat{k} = -\hat{R}_1$ direction with polarization properties given by \hat{n}_b according to

$$\underline{E}_R^i = j\omega\mu \frac{e^{-jkR}}{R} \hat{n}_b e^{jk\hat{k} \cdot \underline{\rho}} \quad (40)$$

$$\underline{H}_R^i = \frac{\hat{k} \times \underline{E}_R^i}{\eta_0} = jk \frac{e^{-jkR}}{R} e^{jk\hat{k} \cdot \underline{\rho}} (\hat{n}_b \times \hat{R}_1) \quad (41)$$

where $k = \omega\mu/\eta_0 = 2\pi/\lambda$ and where $\underline{\rho}$ is the position vector from the origin of coordinates to the source point on S_3 as indicated in Figure 6. The constant C in Equation (39) will be chosen to conform to these explicit expressions for the incident plane wave. When Equation (14) is substituted for \underline{E} in $I_b \Delta l \underline{E} \cdot \hat{n}_b$, there results

$$V_R = \frac{I_b \Delta \ell}{4\pi} \int_S [-j\omega\mu \frac{e^{-jkR}}{R} e^{j\mathbf{k}\hat{\mathbf{k}} \cdot \underline{\rho}} \hat{\mathbf{n}}_b \cdot (\hat{\mathbf{n}} \times \underline{\mathbf{H}}_T) + \hat{\mathbf{n}}_b \cdot (\hat{\mathbf{n}} \times \underline{\mathbf{E}}_T) \\ \times R_1 \frac{jke^{-jkR}}{R} e^{j\mathbf{k}\hat{\mathbf{k}} \cdot \underline{\rho}} + \hat{\mathbf{n}}_b \cdot \nabla\psi_{ff}(\hat{\mathbf{n}} \cdot \underline{\mathbf{E}}_T)] dS \quad (42)$$

where the following asymptotic relations have been used:

$$r \sim R - \underline{R}_1 \cdot \underline{\rho} \quad (43)$$

$$\frac{e^{-jkr}}{r} \sim \frac{e^{-jkR}}{R} e^{j\mathbf{k}\hat{\mathbf{k}} \cdot \underline{\rho}} \quad (44)$$

$$\underline{\nabla}\psi \sim \underline{\nabla}\psi_{ff} = \hat{\mathbf{R}}_1 jk \frac{e^{-jkR}}{R} e^{j\mathbf{k}\hat{\mathbf{k}} \cdot \underline{\rho}} \quad (45)$$

Applying the vector identity $\underline{a} \cdot \underline{b} \times \underline{c} = \underline{b} \cdot \underline{c} \times \underline{a}$ to the first term in the integrand of Equation (42) yields

$$-j\omega\mu \frac{e^{-jkR}}{R} e^{j\mathbf{k}\hat{\mathbf{k}} \cdot \underline{\rho}} \hat{\mathbf{n}}_b \cdot (\hat{\mathbf{n}} \times \underline{\mathbf{H}}_T) = -j\omega\mu \frac{e^{-jkR}}{R} \hat{\mathbf{n}} \cdot \underline{\mathbf{H}}_T \times \hat{\mathbf{n}}_b e^{j\mathbf{k}\hat{\mathbf{k}} \cdot \underline{\rho}} \quad (46)$$

$$= \underline{\mathbf{E}}_T^i \times \underline{\mathbf{H}}_T \cdot \hat{\mathbf{n}} \quad (47)$$

i.e., it is equal to the negative of the second term of the integrand in Equation (39). Repeated application of the same vector identity to the second term in the integrand of Equation (42) yields

$$\hat{\mathbf{n}}_b \cdot ((\hat{\mathbf{n}} \times \underline{\mathbf{E}}_T) \times \hat{\mathbf{R}}_1 \frac{jke^{-jkR}}{R} e^{j\mathbf{k}\hat{\mathbf{k}} \cdot \underline{\rho}}) = \hat{\mathbf{n}} \cdot (\underline{\mathbf{E}}_T \times (jk \frac{e^{-jkR}}{R} e^{j\mathbf{k}\hat{\mathbf{k}} \cdot \underline{\rho}} \hat{\mathbf{R}}_1 \times \hat{\mathbf{n}}_b)) \quad (48)$$

$$= - \underline{\mathbf{E}}_T \times \underline{\mathbf{H}}_T^i \quad (49)$$

i.e., it is equal to the negative of the first term in the integrand of Equation (39). The third term in the integrand of Equation (42) is identically zero since \hat{n}_b is perpendicular to $\nabla\psi_{ff}$. Collecting results yields the final desired result where the complex constant C is chosen to be

$$C = - \frac{I_b \Delta l}{4\pi} \quad (50)$$

to ensure equality.

A concise application of the foregoing analysis is to show that the response of Antenna "a" to the incident plane wave depends only on the incident fields $\underline{E}_R^i, \underline{H}_R^i$ and not on the scattered fields $\underline{E}_{RS}, \underline{H}_{RS}$. Direct examination of the first equality in Equation (39), as well as examination of Equations (47) and (49), reveals that this is indeed the case. The total fields $\underline{E}_R, \underline{H}_R$ on S_3 are given by the superposition of the incident and the scattered fields as

$$\underline{E}_R = \underline{E}_R^i + \underline{E}_{RS} \quad (51)$$

$$\underline{H}_R = \underline{H}_R^i + \underline{H}_{RS} \quad (52)$$

Substituting into the reciprocity integral of Equation (39) yields

$$V_R = C \int_{S_3} (\underline{E}_T \times \underline{H}_R^i - \underline{E}_R^i \times \underline{H}_T) \cdot \hat{n} \, dS + C \int_{S_3} (\underline{E}_T \times \underline{H}_{RS} - \underline{E}_{RS} \times \underline{H}_T) \cdot \hat{n} \, dS \quad (53)$$

The second integral must be identically zero because of the equivalence established explicitly above; also, it must be zero by virtue of the

reciprocity theorem itself as discussed in Section II above following Equation (10).

V. CONCLUSIONS

The theory of radome analysis is based entirely on the reciprocity theorem and the Huygens-Fresnel (or Kirchoff-Huygens) principle, both of which are derivable from Maxwell's equations via a vector Green's theorem and the divergence theorem (Gauss' Law). All methods of radome analysis can be cast in terms of the theory presented to provide a common basis of understanding, to clarify any approximations, and to provide a basis of comparison for the procedures used and numerical results obtained.

The theory presented provides the correct framework in which to think about radome analysis. Its understanding is of paramount importance to the correct development of new analysis methods which may utilize modern numerical methods such as method of moments, GTD, and hybrids of the two. The theory provides the basis for the development of even newer methods of analysis which may rely on special computer architectures or networks. Its presentation here provides a solid theoretical foundation for future thrusts in this important area.

ACKNOWLEDGMENTS

This research was sponsored by the Air Force Office of Scientific Research under Grant AFOSR-77-3469. The United States Government is authorized to reproduce and distribute reprints for governmental purposes notwithstanding any copyright notation hereon.

REFERENCES

1. R. F. Harrington and A. T. Villeneuve, "Reciprocal relations for gyrotropic media", IRE Trans., Vol. MMT-6, pp. 308-310, July 1958.
2. J. A. Stratton and L. J. Chu, "Diffraction theory of electromagnetic waves", Physical Review, Vol. 56, pp. 99-107, July 1939.
3. S. Silver, Microwave Antenna Theory and Design, New York: McGraw-Hill, 1949, pp. 80-84.
4. G. K. Huddleston, "Aperture synthesis of monopulse antenna for radome analysis using limited measured pattern data", submitted to IEEE Trans., AP, September 1980.
5. G. K. Huddleston, H. L. Bassett, and J. M. Newton, "Parametric investigation of radome analysis methods", 1978 IEEE AP-S Symposium Digest, pp. 199-201, 1978.
6. S. Silver, ibid., pp. 522-542.
7. N. R. Kilcoyne, "An approximate calculation of radome boresight error", Proc. USAF/Georgia Inst. of Tech. Symp. on Electromagnetic Windows, pp. 91-111, June 1968.
8. O. Snow, "Discussion of ellipticity produced by radomes and its effects on crossover point position for conically scanning antennas", U. S. Naval Air Development Center, Rpt. E15106, 1951.
9. P. I. Pressel, "Boresight prediction technique", Proc. OSU-WAFC Radome Symposium, 1956.
10. R. E. VanDoeren, "Application of an integral equation method to scattering from dielectric rings", Proc. of the Symposium on Electromagnetic Windows, pp. 113-127, June 1968.
11. G. Tricoles, "Radiation patterns and boresight error of a microwave antenna enclosed in an axially symmetric dielectric shell", J. Opt. Soc. of Amer., 54, No. 9, pp. 1094-1101, Sept. 1964.
12. M. Tavis, "A three-dimensional ray tracing method for the calculation of radome boresight error and antenna pattern distortion", Report No. TOR-0059(56860)-2, Air Force Systems Command, May 1971.
13. D. T. Paris, "Computer-aided radome analysis", IEEE Trans., AP-18, No. 1, pp. 7-15, Jan. 1970.
14. D.C.F. Wu and R. C. Rudduck, "Application of plane wave spectrum representation to radome analysis", Proc. of the Tenth Symposium on Electromagnetic Windows, pp. 46-49, July 1970; also Final Report 2869-4 (AD 772 634), March 1971.

15. E. B. Joy and G. K. Huddleston, "Radome effects on ground mapping radar", Contract DAAH01-72-C-0598, U. S. Army Missile Command, March 1973.
16. Robert Chesnut, "LAMPS radome design", Proc. of the Thirteenth Symposium on Electromagnetic Windows, pp. 73-78, Sept. 1976.
17. G. K. Huddleston and E. B. Joy, "Development of fabrication and processing techniques for laser hardened missile radomes: radome electrical design analysis", MMC Purchase Agreement No. 573712, Martin-Marietta Aerospace, March 1977.
18. K. Siwiak, T. Dowling, L. R. Lewis, "The reaction approach to radome induced boresight error analysis", 1978 Inter. IEEE Symp. Digest, Antennas and Prop., pp. 203-205, May 1978.
19. R. A. Hayward, E. L. Rope, and G. P. Tricoles, "Accuracy of two methods for numerical analysis of radome electromagnetic effects", Proc. of the Fourteenth Symp. on Electromagnetic Windows, pp. 53-55, June 1978.
20. R. E. Collin and F. J. Zucker, Antenna Theory, Part 1, New York: McGraw-Hill, 1961, pp. 94-98.
21. R. F. Harrington, Time-Harmonic Electromagnetic Fields, New York: McGraw-Hill, 1961, pp. 100-110.
22. A. J. Poggio and E. K. Miller, "Integral equation solutions of three-dimensional scattering problems", in Computer Techniques for Electromagnetics, R. Mittra, Ed., New York: Pergamon, 1973, Ch. 4.
23. S. Silver, *ibid.*, p. 63.
24. A.E.H. Love, "The integration of the equations of propagation of electric waves", Philosophical Transactions of the Royal Society of London, Vol. 197-A.287, pp. 1-45, February 1901.
25. R. F. Harrington, *ibid.*, pp. 106-110.
26. S. Silver, *ibid.*, pp. 146-149.
27. R. F. Harrington, Field Computation by Moment Methods, New York: McMillan, 1968.
28. R. A. Hayward, E. L. Rope, and G. Tricoles, "Radome boresight error and its relation to wavefront distortion", Proceedings of 13th Symposium on Electromagnetic Windows, Atlanta, Georgia, pp. 87-91, September 1976.
29. Collin and Zucker, *ibid.*, p. 105.
30. D. T. Paris, E. B. Joy, W. M. Leach, and G. P. Rodrigue, "Basic theory of probe-compensated near-field measurements", IEEE Trans., Vol. AP-26, No. 3, pp. 373-379, May 1978.

APPENDIX B

"Aperture Synthesis of Monopulse Antenna for
Radome Analysis Using Limited Measured Pattern Data"

Submitted for Review for Publication

in

IEEE Transactions of the Antennas and Propagation Society

September 1980

Aperture Synthesis of Monopulse Antenna

For Radome Analysis Using Limited Measured Pattern Data

G. K. Huddleston
School of Electrical Engineering
Georgia Institute of Technology
Atlanta, Georgia 30332
404-894-2928

Abstract

A planar aperture synthesis procedure which predicts measured radiation pattern data accurately and which exploits known physical parameters of the actual antenna is described for use in computer-aided radome analysis. The plane wave spectrum (PWS) representation, with the geometrical optics approximation, is used to characterize radiation from the array of four identical, discrete, conical horn elements that was studied. Solutions for the PWS of each element from measured array patterns over the visible region are presented, and a digital signal processing algorithm is described for extrapolating the aperture-limited PWS into the evanescent region as required to determine the near field of each element. The element near fields, having bounded support, are combined to produce a near field for the complete array. The array near field is used in a computer-aided radome analysis to demonstrate the accuracy to which the measured antenna patterns are predicted for the case of a free space radome. For completeness, comparisons of measured and computed patterns for a tangent ogive Rexolite ($\epsilon_r = 2.54$) radome are presented.

INTRODUCTION

Valid comparisons of the accuracies of radome analysis methods using measured radiation patterns as true data [1] require that each method under consideration be capable of predicting accurately from a suitable antenna near field the antenna patterns measured in the absence of the radome; otherwise, any differences between measured and calculated patterns with the radome in place would be as attributable to the inadequacy of the antenna model as to the radome analysis method itself.

When the measured amplitude and phase of the antenna fields are known over a complete sphere enclosing the antenna, a complete aperture synthesis method such as that described by Ludwig can be used [2]. But when, as in many cases of practical importance, the measured pattern data is limited to amplitude-only, principal plane patterns, a different approach and one which exploits all available information about the antenna being modelled must be used.

Such a method of planar aperture synthesis for the four-horn monopulse antenna of Figure 1 using measured principal plane amplitude patterns of the sum, elevation difference, and azimuth difference channels is described in what follows. The radius ($a = .74\lambda$) and element half-spacing ($d_x = d_y = .95\lambda$) of each vertically (y) polarized conical horn element (10° flare angle) are used in the antenna model to describe radiation from it in the sinusoidal steady state (time variations of the form $e^{j\omega t}$ and suppressed). The aperture fields of each identical element in the four-horn array are

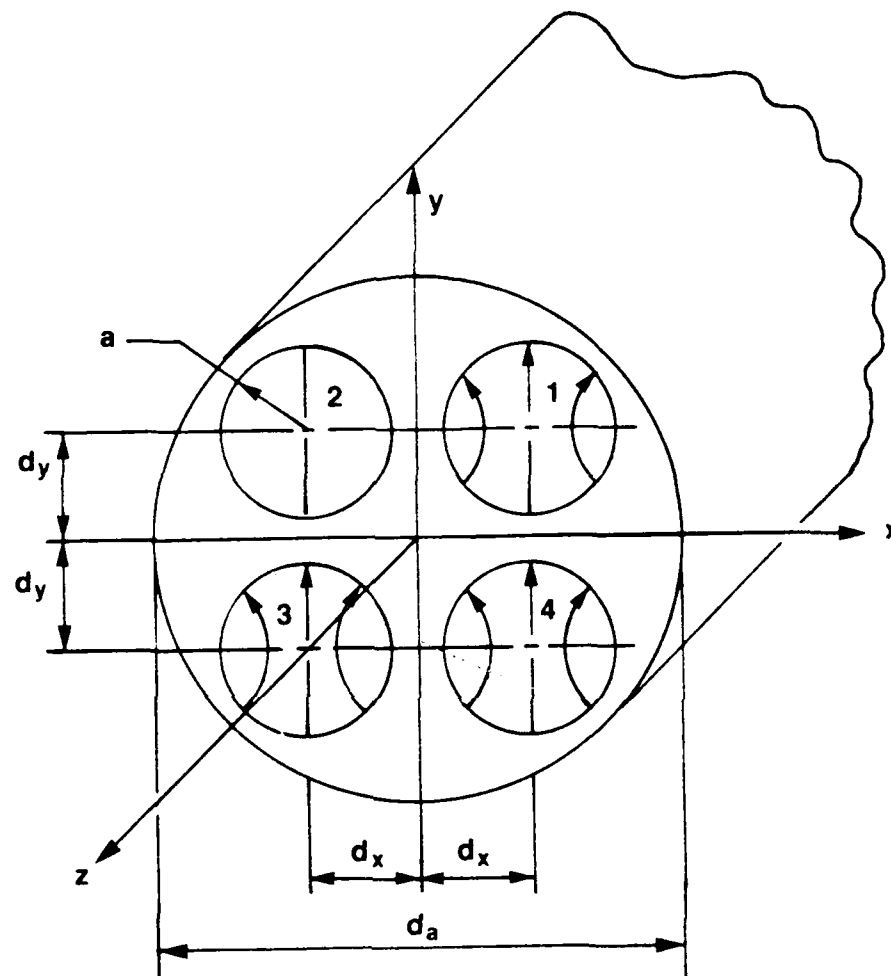


Figure 1. Geometry of Four-Horn Monopulse Antenna.

represented by their plane wave spectra [3] as determined in the principal planes from the measured patterns and the above physical parameters of the actual antenna. The two-dimensional plane wave spectra in the other radiating portions of the wavenumber $k_x k_y$ -plane are determined according to a mathematical model deemed characteristic of the actual element and which utilizes principal plane spectra only; e.g., separable spectra, circularly symmetric spectra, etc. The element plane wave spectra in the non-radiating or evanescent region of the wavenumber plane are found by extrapolating the aperture-limited spectra from the visible to the invisible region using an algorithm described by Papoulis for one-dimensional band-limited functions [4]. The element plane wave spectra so found are then recombined with the array factor to produce the spectra for the complete antenna which, upon Fourier transformation, yields a near field for the antenna which accomplishes the desired result.

This antenna synthesis problem is motivated by an on-going parametric investigation of radome analysis methods [1]. A general theory has been developed, based on the Huygens-Fresnel principle and Lorentz reciprocity, which embodies the various methods of radome analysis [e.g., 5-10]. Computer codes for three typical methods have been implemented. Measured pattern data and boresight error data for three antenna sizes (small, medium, and large) combined in fifteen combinations with five radomes have been obtained to serve as true data in determining the accuracies and ranges of validity of the three methods of analysis. The particular monopulse antenna configuration [11] in Figure 1 was chosen for its ruggedness, ease of fabrication, and ease of duplication in the different physical sizes. Since the perturbations in the patterns and boresight errors caused by the radome are small, it is essential to the success of the research that the actual antennas be accurately modelled in the analyses so that

valid comparisons of the methods can be made. The synthesis procedure was developed specifically for this purpose and for this antenna configuration, but it has wider application and is applicable to more general configurations.

The plane wave spectrum representation of the antenna fields is well suited to the radome analysis application because of the computational efficiency which can accrue as a result of the Fourier transform relations between the aperture fields and the plane wave spectra/far fields. And because of the asymptotic relationships between the far fields and the plane wave spectra, the latter can be mathematically determined from the former, at least over the visible region corresponding to the hemisphere $z > 0$. But before the desired near fields can be determined, it is necessary to assign values to the spectra corresponding to the evanescent or non-radiating modes. Failure to do so may result in a near field which, because it contains only radiating modes, may be too spread out to fit within the confines of the radome for analysis purposes.

In the synthesis procedure here, values are assigned to the evanescent modes by extrapolating the plane wave spectra from the known visible region into the evanescent region. Such extrapolation is valid only for an aperture-limited spectrum; i.e., a spectrum which is the Fourier transform (or inverse transform) of an aperture field which has bounded support. Such a spectrum is an entire function [12] of the (complex) wavenumbers k_x, k_y whose value in one region of the complex k_x and k_y planes can, in principle, be determined by analytic continuation from a known region [13]. The algorithm described by Papoulis provides a practical, computer-aided procedure for implementing the extrapolation; it is also computationally efficient since the Fast Fourier Transform (FFT) algorithm can be exploited.

This synthesis problem is actually an inverse source problem such as that described by Schmidt-Weinmar and Baltes [14] in which prior knowledge about the source plays an important role. It is well known that such problems involve the mathematical questions of existence, uniqueness, and stability of the solution. Small errors in the experimental data, (errors and noise are inevitably present) can lead to large errors in the solution unless suitable stabilizing constraints are imposed; i.e., unless additional prior knowledge can be taken for granted or known to be fact. The procedure described here utilizes a novel combination of known and assumed data, the sum of which provides enough information to produce a stable solution to the inverse problem which fits all the prescribed known data -- but which may not be unique. The question of uniqueness and the amount of information, both prior knowledge and measured data, needed to ensure uniqueness is the subject of a current investigation.

This paper presents the solution for the plane wave spectra of the antenna in terms of the measured patterns and the physical parameters of the antenna. Spectrum functions separable in rectangular and in polar coordinates are presented which permit the specification of the complete radiating spectrum from knowledge of it in only the principal planes. The extrapolation procedure in both one dimension and in two dimensions is detailed and used to effect solutions for a theoretical antenna, whose solution is known exactly for verification purposes, and for the actual antenna. Computer generated results are presented in the forms of radiation pattern comparisons and three-dimensional plots of the near fields and plane wave spectra. To demonstrate applicability and for completeness, some radome analysis results are presented.

THEORETICAL DERIVATIONS

The synthesis procedure is carried out independently in the two principal planes to determine the plane wave spectra $A_{xe}(k_x, k_y)$, A_{ye} , and aperture fields $E_{xe}(x, y)$, E_{ye} of each identical element in the four-horn array of Figure 1. The general expression for the radiation field of the array may be written as a product of the element field and the array factor as

$$E_{eff}(k_x, k_y) = E_{eff}(k_x, k_y) [a_1 e^{jk_o(dk_x + dk_y)} + a_2 e^{jk_o(-dk_x + dk_y)} + a_3 e^{jk_o(-dk_x - dk_y)} + a_4 e^{jk_o(dk_x - dk_y)}] \quad (1)$$

where $k_o = 2\pi/\lambda$, $j = \sqrt{-1}$, the a_i 's are the complex excitation coefficients of the elements numbered and spaced as shown in Figure 1, E_{eff} is the radiation (electric) field of the element, and the normalized wavenumbers k_x , k_y are related to spherical angles θ , ϕ of Figure 2 by

$$k_x = \sin\theta \cos\phi \quad (2)$$

$$k_y = \sin\theta \sin\phi, \quad (3)$$

at least for the visible region defined by $\sqrt{k_x^2 + k_y^2} \leq 1$

The three monopulse channels of the antenna are formed by phasing the elements appropriately. In the ideal case, $|a_i| = 1$ for $i = 1-4$. For the sum (Σ) channel, all elements are assigned equal phase. For the elevation difference (Δ_{EL}) channel, $a_1 = a_2 = -a_3 = -a_4$. For the azimuth difference (Δ_{AZ}) channel, $a_1 = a_3 = -a_2 = -a_4$. For perfect assignment of the excitation coefficients, there results

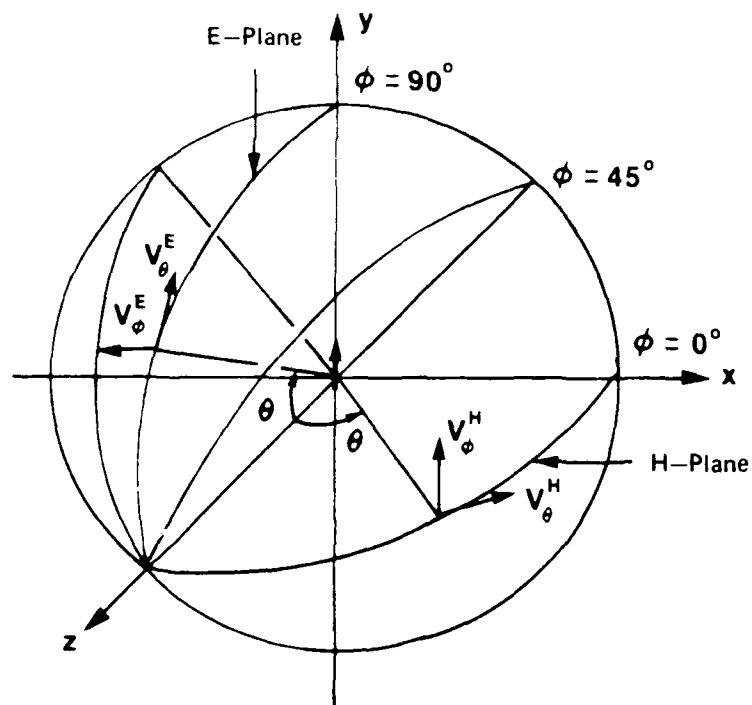


FIGURE 2. COORDINATE SYSTEM FOR ANTENNA PATTERN MEASUREMENTS ON VERTICALLY POLARIZED ANTENNA.

$$\underline{E}_{eff} = \underline{E}_{eff}(k_x, k_y) (4 \cos k_0 d \cos k_x \cos k_0 d \cos k_y) \quad (4)$$

$$\underline{E}_{eff12} = \underline{E}_{eff}(k_x, k_y) (4 \cos k_0 d \cos k_x \sin k_0 d \cos k_y)$$

$$\underline{E}_{eff12} = \underline{E}_{eff}(k_x, k_y) (4 \sin k_0 d \cos k_x \cos k_0 d \cos k_y) \quad (6)$$

In the non-ideal case encountered in practice, the excitation coefficient values may vary somewhat from the ideal values so that the complex array factor of Equation (1) must be used in solving for the element field and plane wave spectra of measured sum and difference patterns.

The radiation field of the element is related to its plane wave spectra according to [15]

$$\begin{aligned} \underline{E}_{eff}(k_x, k_y) = & \hat{x} [(1+k_z^2-k_x^2) A_{xe} - k_x k_y A_{ye}] \\ & + \hat{y} [-k_x k_y A_{xe} + (1+k_z^2-k_y^2) A_{ye}] \\ & + \hat{z} [-k_x (1+k_z) A_{xe} - k_y (1+k_z) A_{ye}] \end{aligned} \quad (7)$$

where $k_z = \sqrt{1-k_x^2-k_y^2}$. The geometrical optics approximation [16] has been assumed for the aperture fields in the conical horn element; viz.,

$$\underline{H}_{ap} = \frac{\hat{z} \times \underline{E}_{ap}}{\eta} \quad (8)$$

where \hat{x} , \hat{y} , \hat{z} are unit vectors in the rectangular coordinate system of Figure 2 and η is the wave impedance. In Equation (7), the radiation factor of the form e^{-jkr}/r has been suppressed where r is the radial

distance from the origin of antenna coordinates to the far-field measurement sphere of Figure 2.

Equation (7) may also be written in terms of the transverse spherical components as

$$E_{\text{eff}}(k_x, k_y) = \frac{(1+k_z)}{\sqrt{k_x^2 + k_y^2}} [\hat{\theta}(k_x A_{xe} + k_y A_{ye}) + \hat{\phi}(-k_y A_{xe} + k_x A_{ye})] \quad (9)$$

which is a form more suitable to solution for A_{xe}, A_{ye} in terms of the measured transverse components E_{θ}, E_{ϕ} or the related measured quantities V_{θ}, V_{ϕ} defined by

$$V_{\theta} = \begin{cases} E_{\theta} & , \quad k_x > 0 \\ -E_{\theta} & , \quad k_x < 0 \end{cases}$$

$$V_{\phi} = \begin{cases} E_{\phi} & , \quad k_x = 0 \\ -E_{\phi} & , \quad k_x \neq 0 \end{cases} \quad (11)$$

For $k_x = 0$ (E-plane), the definitions above apply when k_y is substituted for k_x . Let AF_i , $i=1,2,3$, denote the array factors associated with the $\Delta, \Delta_{EL}, \Delta_{AZ}$ channels, respectively, modelled in Equation (1). Then the solutions for the element spectra are given by

$$A_{xe}(k_x, k_y) = \frac{k_x V_{\theta i} - k_y V_{\phi i}}{(1+k_z) \sqrt{k_x^2 + k_y^2} AF_i} \quad (12)$$

$$A_{ye}(k_x, k_y) = \frac{k_y V_{\theta i} + k_x V_{\phi i}}{(1+k_z) \sqrt{k_x^2 + k_y^2} AF_i} \quad (13)$$

for all k_x, k_y such that $0 \leq k_z \leq 1$. At the pole, $k_z = 1$ and the spectra may be found from the sum channel measured voltages as

$$A_{xe}(0,0) = V_{\phi 1}^H(0,0) = -V_{\phi 1}^E(0,0) \quad (14)$$

$$A_{ye}(0,0) = V_{\phi 1}^H(0,0) = V_{\phi 1}^E(0,0) \quad (15)$$

where the superscripts denote the conventional E and H planes [17]. The general expressions in Equations (12) and (13) can be specialized to these principal planes as follows:

H-Plane ($k_y = 0$):

$$A_{xe}(k_x, 0) = \frac{V_{\theta i}^H(k_x)}{(1 + \sqrt{1 - k_x^2}) AF_i} \quad (16)$$

$$A_{ye}(k_x, 0) = \frac{V_{\phi i}^H(k_x)}{(1 + \sqrt{1 - k_x^2}) AF_i} \quad (17)$$

E-Plane ($k_x = 0$):

$$A_{xe}(0, k_y) = \frac{-V_{\phi i}^E(k_y)}{(1 + \sqrt{1 - k_y^2}) AF_i} \quad (18)$$

$$A_{ye}(0, k_y) = \frac{V_{\theta i}^E(k_y)}{(1 + \sqrt{1 - k_y^2}) AF_i} \quad (19)$$

When numerically evaluating Equations (16)-(19), the channel index i is chosen on the basis of highest signal level. For example, the E channel ($i=1$) provides the best data for small $|k_x|$ in the H-plane; however, as $|k_x|$ increases, the sum channel amplitude decreases toward the first null in the array factor AF , while the Δ_{AZ} channel amplitude increases toward its peak at $k_x \approx \pm \sin^{-1}((4d_x/\lambda)^{-1})$. When alternating between the data sets, it is important to ensure that the measured difference channel data is correctly normalized with respect to the sum data as dictated by the model in Equation (1). For ideal excitation coefficients, the ratio of difference channel response to sum channel response is given in each principal plane by

H-Plane:

$$\frac{\Delta_{AZ}(k_x, 0)}{\Sigma(k_x, 0)} = j \tan k_o d_x k_x \quad (20)$$

E-Plane:

$$\frac{\Delta_{EL}(0, k_y)}{\Sigma(0, k_y)} = j \tan k_o d_y k_y \quad (21)$$

These relationships can be used to adjust the data for consistent solutions of the element spectra.

The measured quantities $V_{\theta_1}, V_{\theta_2}, \dots$ in Equations (16)-(19) are complex quantities usually measured using a vector amplitude receiver. In those myriad cases where far-field probe data are not valid due to range imperfections, unstable microwave sources, etc., some assumption must be made in assigning phase values to the measured amplitude data at each angular direction. In this investigation, phase data were assigned as dictated by the array factor for each channel. The phase of the

element was assumed constant. The phase reconstruction problem [16] was beyond the scope of the present work.

In practice, the excitation coefficients a_i will differ from their ideal values to produce asymmetries in the measured patterns. Values of the excitation coefficients based on the asymmetries in the sum patterns may be found, in paired combinations, as

$$a_{14} = (a_1 + a_4) = \frac{8(e^{j\psi} V_{\phi 1}^H(k_x) - e^{-j\psi} V_{\phi 1}^H(-k_x))}{(e^{j2\psi} - e^{-j2\psi})(1 + k_z)A_{ye}(k_x, 0)} \quad (22)$$

$$a_{23} = (a_2 + a_3) = \frac{8(e^{j\psi} V_{\phi 1}^H(-k_x) - e^{-j\psi} V_{\phi 1}^H(k_x))}{(e^{j2\psi} - e^{-j2\psi})(1 + k_z)A_{ye}(-k_x, 0)} \quad (23)$$

$$a_{12} = (a_1 + a_2) = \frac{8(e^{j\psi} V_{\theta 1}^E(k_x) - e^{-j\psi} V_{\theta 1}^E(-k_x))}{(e^{j2\psi} - e^{-j2\psi})(1 + k_z)A_{ye}(0, k_x)} \quad (24)$$

$$a_{34} = (a_3 + a_4) = \frac{8(e^{j\psi} V_{\theta 1}^E(-k_x) - e^{-j\psi} V_{\theta 1}^E(k_x))}{(e^{j2\psi} - e^{-j2\psi})(1 + k_z)A_{ye}(0, -k_x)} \quad (25)$$

where

$$\psi = k_o d k_x = k_o d k_y \quad (26)$$

$$k_z = \sqrt{1 - k_x^2} \quad (27)$$

and where $k_x = \sin\theta$ is a conveniently chosen point in the sum pattern principal planes, such as the angle corresponding to the peak of the first sidelobe. It is noted that the values of A_{ye} appearing in Equations (22)-

(25) depend on the excitation coefficients; hence, an iterative procedure is indicated. The individual excitation coefficients can then be found, to within a constant, from the four above equations. For definiteness, a value of $(1+j0)$ may be assigned to a_1 . The solutions for the other coefficients follow as:

$$a_2 = a_{12} - 1 \quad (26)$$

$$a_3 = a_{34} - a_{14} + 1 \quad (29)$$

$$a_4 = a_{14} - 1 \quad (30)$$

The near fields of the element can be found from the principal plane PWS via Fourier transformation only for the special case of rectangularly separable spectra; i.e.,

$$A_{xe}(k_x, k_y) = p_x(k_x) q_x(k_y) \quad (31)$$

$$A_{ye}(k_x, k_y) = p_y(k_x) q_y(k_y) \quad (32)$$

In such case the near fields are also separable and given by

$$c_1 E_{xenf}(x, y) = c_1 P_x(x) Q_x(y) = q_x(0) p_x(0) F\{p_x(k_x)\} F\{q_x(k_y)\} \quad (33)$$

$$c_2 E_{yenf}(x, y) = c_2 P_y(x) Q_y(y) = q_y(0) p_y(0) F\{p_y(k_x)\} F\{q_y(k_y)\} \quad (34)$$

where $F\{\}$ denotes Fourier transform and where constants c_1 and c_2 are given by

$$c_1 = p_x(0) q_x(0) = \frac{V_{\theta 1}^H(0)}{8} \quad (32)$$

$$c_2 = p_y(0) q_y(0) = \frac{V_{\phi 1}^H(0)}{8} \quad (33)$$

The Fourier transformation above implies that the spectra are known for all k_x (k_y) on the real line; however, Equations (16)-(19) produce solutions only in the visible region $|k_x| \leq 1$, $|k_y| \leq 1$ of the principal planes. The extrapolation technique for assigning values to the spectra outside the visible region will be deferred until after the discussion immediately below concerning another type of separability for spectra and near fields which will be applied during the synthesis procedure.

The TE_{11} circular waveguide mode (y-polarized) provides a model for an element near field that is separable in cylindrical coordinates ρ and ϕ , and which depends only on knowledge of the principal plane PWS. Assume that the element near field can be written as

$$\underline{E}_{nf}(\rho, \phi) = \hat{\rho} f_{\rho}(\rho) g_{\rho}(\phi) + \hat{\phi} f_{\phi}(\rho) g_{\phi}(\phi) \quad (37)$$

Convert to rectangular coordinates and assume, as in the case of the TE_{11} waveguide mode, that

$$g_{\rho}(\phi) = \sin\phi \quad (38)$$

$$g_{\phi}(\phi) = \cos\phi \quad (39)$$

The element (tangential) near field can then be expressed in rectangular coordinates as

$$\underline{E}_{nf}(x,y) = \hat{x} \frac{f_{\rho}-f_{\phi}}{2} \sin 2\phi + \hat{y} \left(\frac{f_{\rho}+f_{\phi}}{2} - \frac{f_{\rho}-f_{\phi}}{2} \cos 2\phi \right) \quad (40)$$

where $x=\rho\cos\phi$, $y=\rho\sin\phi$ as usual. Inverse Fourier transform these rectangular components to yield integrals

$$A_x(k_x, k_y) = \int_0^a \frac{f_{\rho}-f_{\phi}}{2} \rho d\rho \int_0^{2\pi} \sin 2\phi e^{j2\pi\rho k_{\rho} \cos(\phi-\xi)} d\phi \quad (41)$$

$$\begin{aligned} A_y(k_x, k_y) &= \int_0^a \frac{f_{\rho}+f_{\phi}}{2} \rho d\rho \int_0^{2\pi} e^{j2\pi\rho k_{\rho} \cos(\phi-\xi)} d\phi \\ &\quad - \int_0^a \frac{f_{\rho}-f_{\phi}}{2} \rho d\rho \int_0^{2\pi} \cos 2\phi e^{j2\pi\rho k_{\rho} \cos(\phi-\xi)} d\phi \end{aligned} \quad (42)$$

Carry out the integrations in ϕ [19] to obtain

$$A_x(k_x, k_y) = -2\pi \frac{k_x k_y}{k_{\rho}^2} H_0(k_{\rho}) \quad (43)$$

$$A_y(k_x, k_y) = \pi H_0(k_{\rho}) + \pi \frac{k_x^2 - k_y^2}{k_{\rho}^2} H_2(k_{\rho}) \quad (44)$$

where $k_{\rho} = \sqrt{k_x^2 + k_y^2}$ and where the Hankel transforms H_0 , H_2 are defined by [20]

$$H_0(k_\rho) \triangleq \int_0^a (f_\rho + f_\phi) J_0(k_\rho \rho) \rho d\rho \quad (45)$$

$$H_2(k_\rho) \triangleq \int_0^a (f_\rho - f_\phi) J_2(k_\rho \rho) \rho d\rho \quad (46)$$

Specialize Equations (43) and (44) to the principal planes, and solve the resulting system of equations for H_0 , H_2 to yield

$$H_0(k_\rho) = \frac{A_y(k_\rho, 0) + A_y(0, k_\rho)}{2\pi} \quad (47)$$

$$H_2(k_\rho) = \frac{A_y(k_\rho, 0) - A_y(0, k_\rho)}{2\pi} \quad (48)$$

Thus, the two-dimensional plane wave spectra A_x, A_y are expressible in terms of only the principal plane spectra via Equations (43)-(48).

Since the assumed trigonometric variations of g_ρ, g_ϕ in Equations (38) and (39) do not produce any x-component of near field along $x=0$ or $y=0$, a similar analysis can be carried out for an orthogonal TE-type mode which will account for the presence of such cross-polarized components. Write the total element fields as the sum of two components

$$\underline{E}_{\text{enf}} = \hat{\rho} (E'_\rho + E'_\rho) + \hat{\phi} (E'_\phi + E'_\phi) \quad (49)$$

where E'_ρ, E'_ϕ are given in Equation (37) and where

$$E'_\rho = f'_\rho(\rho) g'_\rho(\phi) = f'_\rho \cos\phi \quad (50)$$

$$E'_\phi = f'_\phi(\rho) g'_\phi(\phi) = f'_\phi \sin\phi \quad (51)$$

Follow through with the analysis and define Hankel transforms G_0 , G_2 by

$$G_0(k_\rho) = \int_0^a (f'_\rho - f'_\phi) J_0(k_\rho \rho) \rho d\rho \quad (52)$$

$$G_2(k_\rho) = \int_0^a (f'_\rho + f'_\phi) J_2(k_\rho \rho) \rho d\rho \quad (53)$$

Combine all results for the two orthogonal modes to yield the following expressions for the element plane wave spectra in terms of the principal plane spectra $A_{xe}^H(k_\rho)$, $A_{xe}^E(k_\rho)$, $A_{ye}^H(k_\rho)$, $A_{ye}^E(k_\rho)$:

$$A_{xe}(k_x, k_y) = \frac{A_{xe}^H + A_{xe}^E}{2} + \frac{k_x^2 - k_y^2}{k_\rho^2} \left(\frac{A_{xe}^H - A_{xe}^E}{2} \right) + \frac{k_x k_y}{k_\rho^2} (A_{ye}^E - A_{ye}^H) \quad (54)$$

$$A_{ye}(k_x, k_y) = \frac{A_{ye}^H + A_{ye}^E}{2} + \frac{k_x^2 - k_y^2}{k_\rho^2} \left(\frac{A_{ye}^H - A_{ye}^E}{2} \right) + \frac{k_x k_y}{k_\rho^2} (A_{xe}^H - A_{xe}^E) \quad (55)$$

The above two equations constitute a reasonable model for the plane wave spectra of a circular element such as that shown in Figure 1. The principal plane spectra in these equations are found from measured principal plane patterns via Equations (16)-(19). Note that the above equations reduce identically to the measured spectra in the principal planes. Note also that the model is based on the characteristic modes of a circular aperture geometry and, in the absence of complete measured data which could perhaps determine exactly the plane wave spectra off the principal planes, this model is more suitable for the antenna described than is the model of Equations (31)-(32) which assumes rectangular

separability. Strictly speaking, the latter would more suitable for use with a rectangular element geometry, but does find application in the extrapolation procedure described next.

EXTRAPOLATION PROCEDURE

The extrapolation procedure is best explained in one dimension before extending it to the two-dimensional case. The objective of the procedure is to assign values to the evanescent modes in the plane wave spectrum of the element such that the known spectrum in the visible region is preserved and such that the near field of the element is restricted to a finite portion of the xy-plane. Results are presented in this section which demonstrate the algorithm for both an ideal case and a case which uses measured data.

The flow chart in Figure 3 summarizes the extrapolation procedure for the case of plane wave spectrum $A_x(k_x)$ and its corresponding near field $E_x(x) = F\{A_x(k_x)\}$. The zeroeth estimate to the actual spectrum is the portion known only over radiating wavenumbers as defined by

$$A_{x0}(k_x) = \begin{cases} A_x(k_x) & , \quad |k_x| \leq 1 \\ 0 & , \quad \text{elsewhere} \end{cases} \quad (5c)$$

The known length $2a$ of the interval over which the near field is non-zero, and a lower bound $1-\epsilon$ on the fraction of energy in the near field which must be contained in this interval for an acceptable solution, constitute the remaining elements of input data.

The first estimate E'_{x0} of the near field is found by Fourier transformation of A_{x0} . Due to the lack of radiating modes in the spectra, the near field will be spread out in x . That portion lying

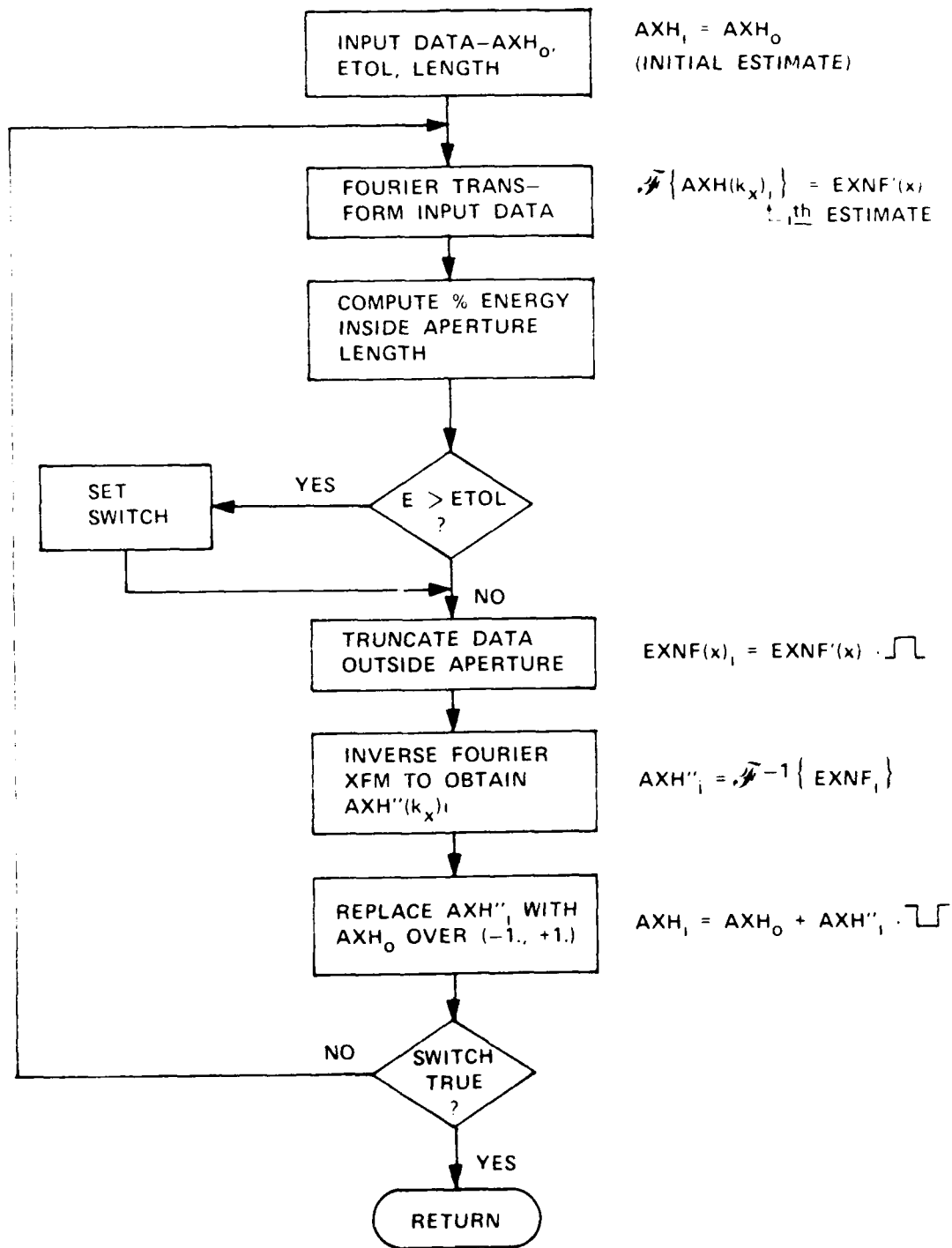


FIGURE 3. FLOW CHART FOR EXTRAPOLATION ALGORITHM.

outside $|x| \leq a$ is then truncated so that $E_{x0} = E'_{x0} p_a(x)$ results, where $p_a(x)$ is the rectangular function whose value is unity for $|x| \leq a$ and zero elsewhere. The resulting near field E_{x0} is inverse Fourier transformed to produce the spectrum $A'_{x1}(k_x)$ which does contain non-zero evanescent modes due to the bounded support of E_{x0} . The evanescent modes of A'_{x1} are added to the radiating modes A_{x0} to produce the first-order spectrum $A_{x1} = A_{x0} + A'_{x1} \bar{p}_1(k_x)$ where $\bar{p}_1(k_x)$ is the complement of the rectangular function whose value is unity for $|x| > a$ and zero for $|x| \leq a$. The process is repeated until the fraction of energy in the near field $E_{x1}(x)$ on the interval $|x| \leq a$ exceeds the lower bound specified. The FFT algorithm is used to effect the Fourier transformations.

The algorithm was first tested on an ideal four-horn monopulse array (Figure 1) where a TE_{11} circular waveguide mode was assumed present in each element. The mode was y-polarized but then rotated by $\alpha = 5^\circ$ counterclockwise so that a small x-component of radiated field would be present. The far fields of the array were computed at 2° increments in the principal planes for all three channels over a dynamic range of 40 decibels. These data were used as the "measured" data V_{ei} , $V_{\phi i}$ in Equations (16)-(19) to produce element spectra $A_{xe}^H(k_x)$, $A_{ye}^H(k_x)$, $A_{xe}^E(k_y)$, $A_{ye}^E(k_y)$ over the visible region in each plane at 2° increments in polar angle θ . Since the discrete Fourier transform relationship between spectrum and near field requires samples of the spectra at equal increments in wavenumber $k_x = \sin \theta$, a Whittaker-Shannon expansion [21] was used to Fourier interpolate the spectrum samples at equal angle; i.e.,

$$A(\theta) = \sum_{m=1}^N A(\theta_m) \frac{\sin \left(\pi N \frac{\theta - \theta_m}{2 \theta_{\max}} \right)}{\pi N \frac{\theta - \theta_m}{2 \theta_{\max}}} \quad (57)$$

where $\theta = \sin^{-1} k_x$, N = number of angular samples (91), and θ_{\max} = angle corresponding to the N th sample (90°). The interpolated spectra were then operated on in turn by the extrapolation algorithm.

Some computed results are shown in Figure 4 where comparisons of the true and synthesized near fields of the element in the $x=0$ plane are presented. The true x and y field components are simply those of the rotated TE_{11} mode. After twenty-one iterations of the extrapolation algorithm, the concentration factors for the x and y components were $\epsilon_x^E = .013$ and $\epsilon_y^E = .330 \times 10^{-4}$, respectively. (In the $y=0$ plane, slightly better results were obtained; i.e., $\epsilon_x^H = .0153$, $\epsilon_y^H = .982 \times 10^{-5}$). The half-length of the interval occupied by the element was $a = .74136\lambda$. The algorithm was quite successful in concentrating the near field into the desired interval and in predicting the spatial variation of the near field reasonably well. The sample spacing in the near field was $\Delta y = \lambda/8$.

The element near fields in Figure 4 were (inverse) Fourier transformed to produce the corresponding spectra at equal wavenumber over the range $|k_y| \leq k_{y\max} = (2 \Delta y / \lambda)^{-1} = 4$. The spectra were then Fourier interpolated, to produce their values at 2° increments over the range $|\theta| \leq 90^\circ$ according to

$$A(k_y) = \sum_{m=1}^N A(k_{ym}) \frac{\sin(\pi N \frac{k_y - k_{ym}}{2 k_{y\max}})}{\pi N \frac{k_y - k_{ym}}{2 k_{y\max}}} \quad (58)$$

The interpolated values were used in the antenna model of Equation (1) to produce the sum channel E-plane patterns shown in Figure 5. Differences between the true and synthesized primary E_θ^E components are hardly

LEGEND

$E_y(0,y)$

$E_y'(0,y)$

$E_x(0,y)$

$E_x'(0,y)$

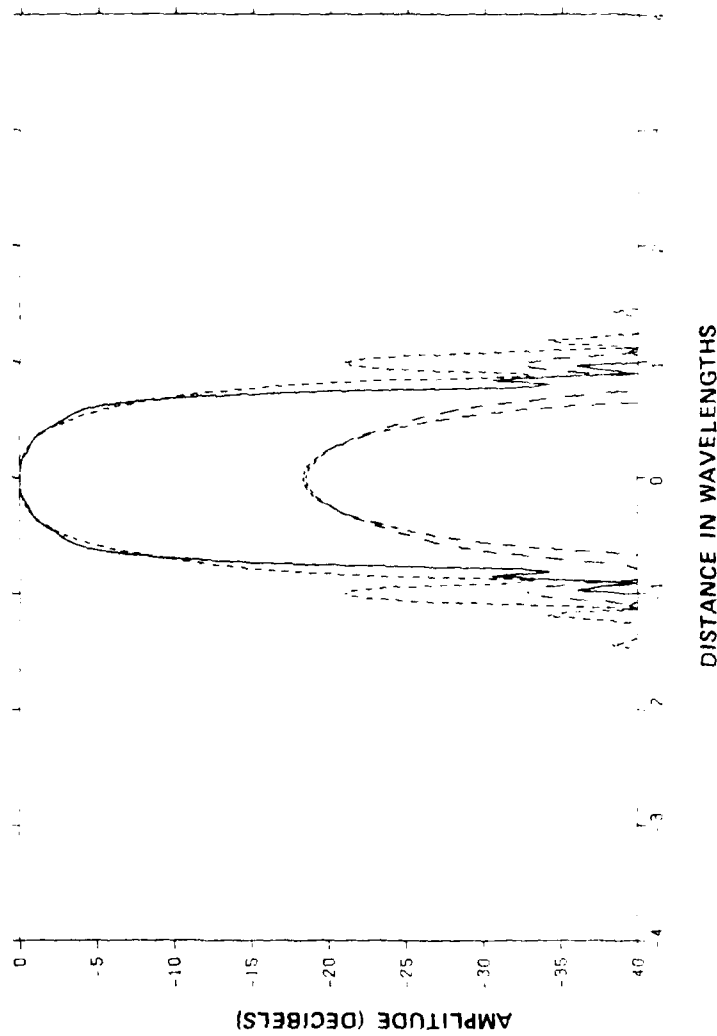


FIGURE 4. COMPARISONS OF TRUE AND SYNTHESIZED (') NEAR FIELDS OF THEORETICAL FOUR-HORN MONOPULSE ANTENNA ELEMENT ($\alpha = 5^\circ$).

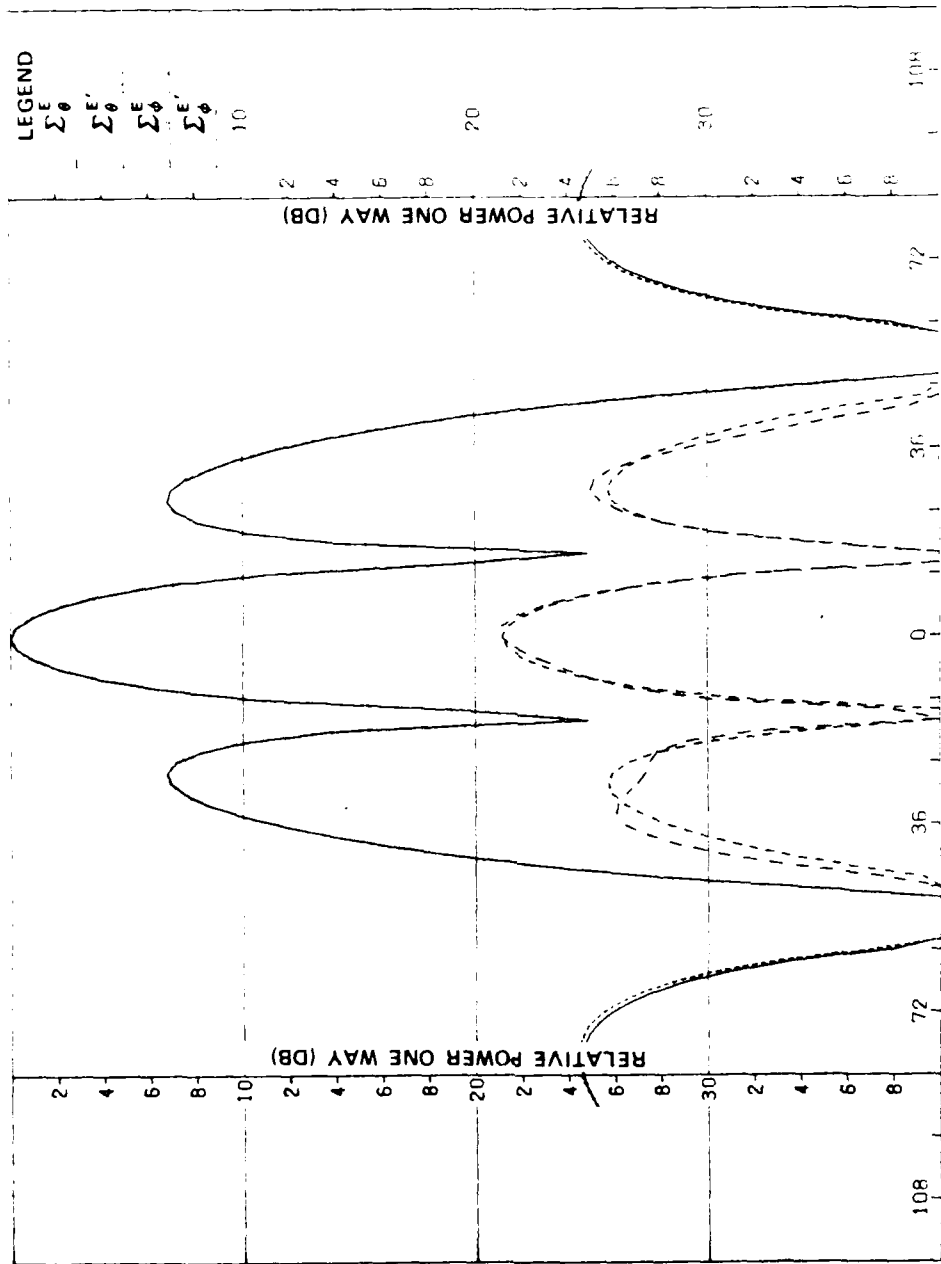


FIGURE 5. COMPARISONS OF TRUE AND SYNTHESIZED (') E-PLANE SUM PATTERNS OF THEORETICAL FOUR-HORN MONOPULSE ANTENNA ($\alpha = 5^\circ$).

discernable except at very wide angles. Good agreement is obtained for the cross E_{ϕ}^E component where all amplitude levels are less than -20 dB. Similar results were obtained in the H-plane and for the other two channels. In conclusion, the synthesis procedure works quite well in one dimension for theoretical data having a dynamic range of 40 decibels.

The one-dimensional synthesis procedure was next tested using principal plane patterns obtained at 35 GHz for the actual antenna of Figure 1. Figure 6 shows the first and final estimates of the element near field in the $x=0$ plane. After 51 iterations of the extrapolation algorithm, the E-plane concentration factors were $\epsilon_x^E = .069$ and $\epsilon_y^E = .38 \times 10^{-3}$. (The H-plane concentration factors were $\epsilon_x^H = .508$ and $\epsilon_y^H = .494 \times 10^{-2}$.) The sample spacing was $\Delta y = .025\lambda$, yielding a maximum wavenumber $k_{y\max} = 20$ for $N=256$ samples over the total interval of 6.4λ . Referring to Figure 6, it is seen that the algorithm successfully concentrated the near field into the interval $|y| \leq a = .74136\lambda$ as desired.

Figure 7 shows comparisons of the measured patterns with those synthesized from the extrapolated element spectra as explained above for the ideal array. The agreement is quite good in the E-plane. Similar results were obtained for the H-plane and for the other two channels. In conclusion, the synthesis procedure works well for measured, one-dimensional data having a 40-dB dynamic range.

TWO DIMENSIONAL EXTRAPOLATION

The one dimensional results could be used through Equations (31) and (32) to generate two-dimensional spectra and near fields; however, if the $\rho\phi$ -separability model is used as preferred, then the extrapolation

LEGEND
FIRST
FINAL

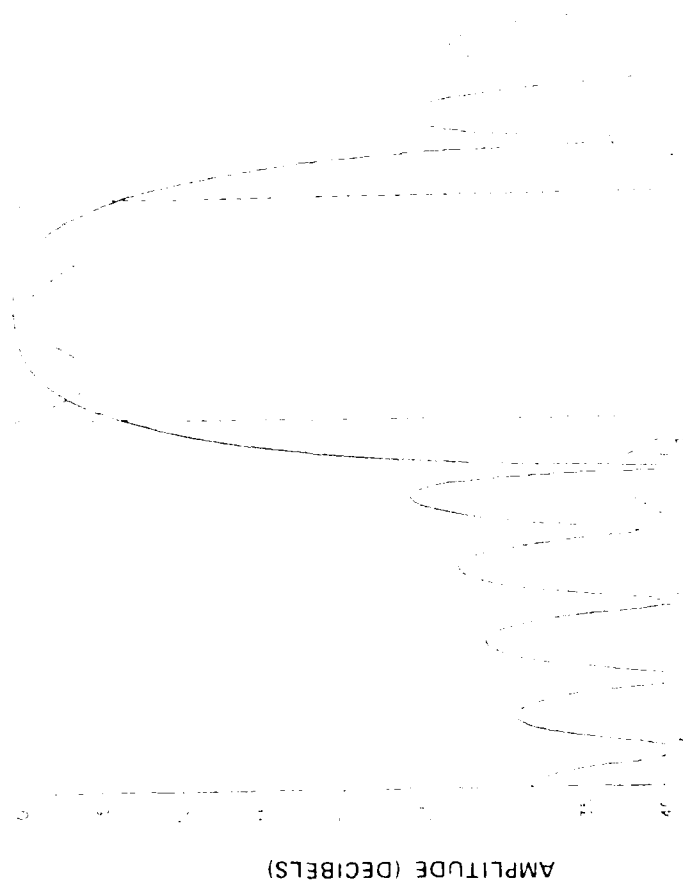


FIGURE 6. FIRST AND FINAL ESTIMATES OF APERTURE FIELD OF ACTUAL ELEMENT IN E-PLANE

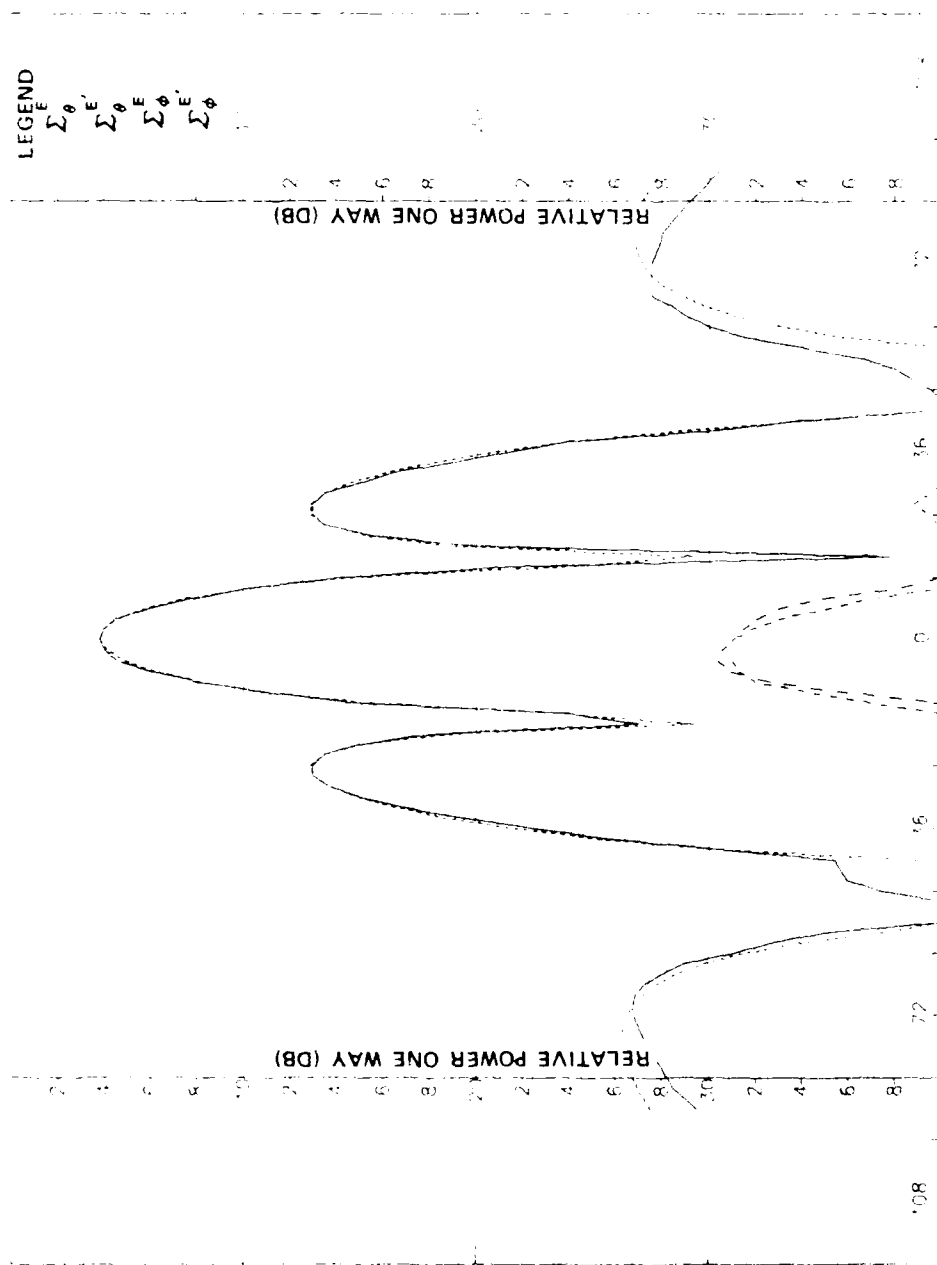


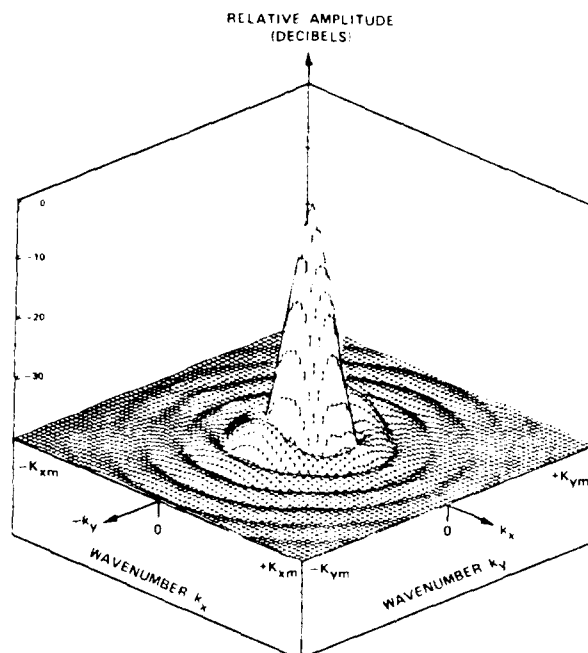
FIGURE 7. COMPARISONS OF MEASURED AND SYNTHESIZED (') E-PLANE SUM PATTERNS OF ACTUAL FOUR-HORN MONOPULSE ANTENNA.

procedure must be carried out in two dimensions.* This section presents results of two-dimensional synthesis of the element spectra and fields of the antenna in Figure 1 using measured principal plane patterns.

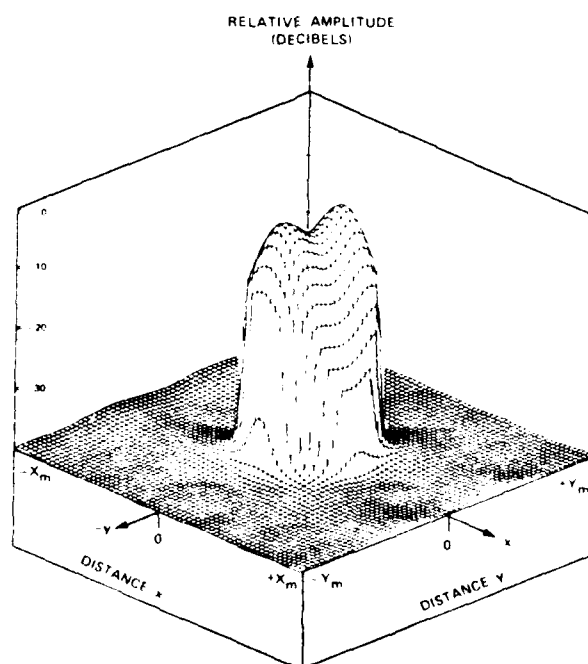
Figure 8 shows the element near field $E_{ye}(x,y)$ and the corresponding plane wave spectrum $A_{ye}(k_x, k_y)$ obtained using the 2-D extrapolation algorithm. The element principal plane spectra were first determined via Equations (16)-(19) from the measured data. These results were then used in Equations (54) and (55) to generate the 2-D plane wave spectra over the visible region $k_x^2 + k_y^2 \leq 1$. The extrapolation algorithm was then applied to each 2D spectrum in turn using a 2-D Fast Fourier Transform. After eleven iterations, the concentration factors were $\epsilon_x = .065$ and $\epsilon_y = .028$; i.e., for the y-component $E_{ye}(x,y)$, 98.2% of the near-field energy was concentrated in the circular element region of radius $a = .74316\lambda$. A square array of 64×64 samples spaced at $\Delta x = \Delta y = .07031\lambda$ and resulting in $k_{x\max} = k_{y\max} = 7.11$ was used for each component. An exponential window was used to limit the near fields to the circular region.

The resulting element spectra were next combined via Equations (1) and (9) to produce the 2D plane wave spectra for the three monopulse channels. Each spectra was then Fourier transformed to obtain the corresponding near fields. Some results for the sum channel are presented in Figure 9. The PWS $A_y^\Sigma(k_x, k_y)$ shown in Figure 9(a) has maximum wavenumbers $k_{x\max} = k_{y\max} = 3.56$. Although no extrapolation was applied to the PWS containing the array factor, the actual measured spectra in the principal planes were inserted directly into the final PWS to guarantee close agreement with measured patterns as extracted from the 2-D PWS.

*One-dimensional extrapolation could possibly be used by utilizing the Hankel transform in place of the Fourier transform.

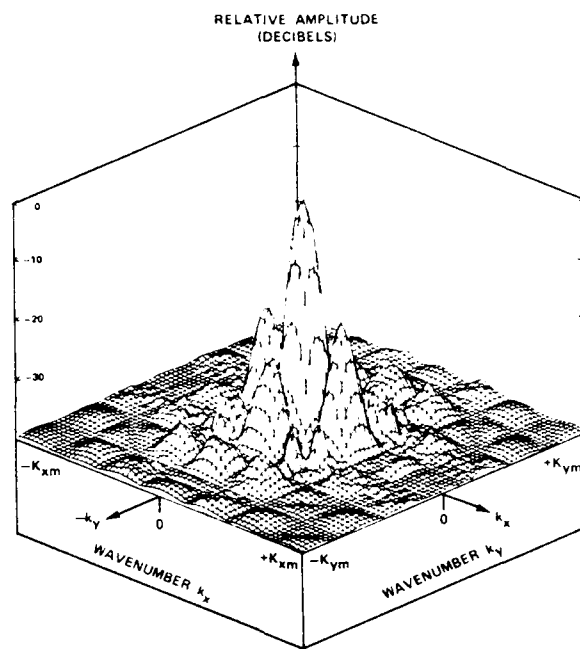


(a) Plane Wave Spectrum.

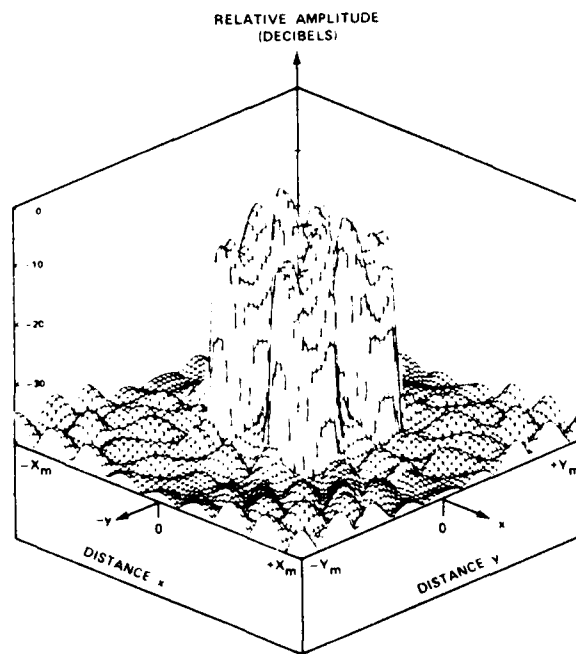


(b) Near Field.

FIGURE 8 PLANE WAVE SPECTRUM $A_y(k_x, k_y)$ AND NEAR FIELD $E_{y\text{nf}}(x, y)$ OF ELEMENT



(a) Plane Wave Spectrum.



(b) Near Field

FIGURE 9 PLANE WAVE SPECTRUM AND NEAR FIELD OF Y-COMPONENT OF FOUR-HORN MONOPULSE ARRAY

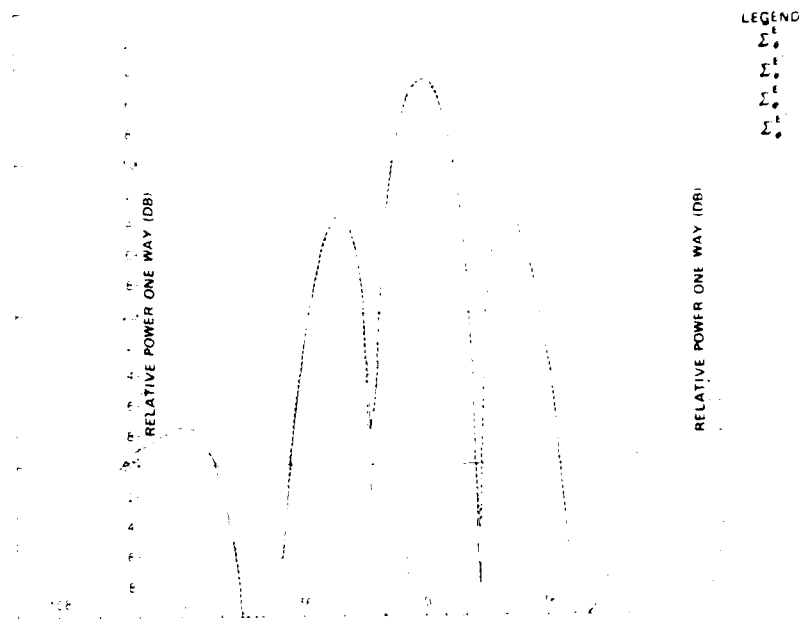
Figure 9(b) shows the y-component of the synthesized near field of the four-horn monopulse antenna at 64×64 samples spaced at $\Delta x = \Delta y = .14045\lambda$. The near fields of the four circular elements are clearly visible, and the vast majority of the near-field energy is concentrated in the central portion of the array.

When selected cuts were extracted from the 2-D phase wave spectra of the sum channel and used in Equation (9), the patterns of Figure 10 resulted. Agreement between the measured and synthesized E-plane sum patterns shown in Figure 10(a) is excellent. But perhaps more importantly, the agreement in the $\phi=45^\circ$ plane is also excellent as shown in Figure 10(b) -- facts which attest to the apparent correctness of the underlying assumptions used throughout the synthesis procedure. Similar results were obtained for the other planes and other channels.

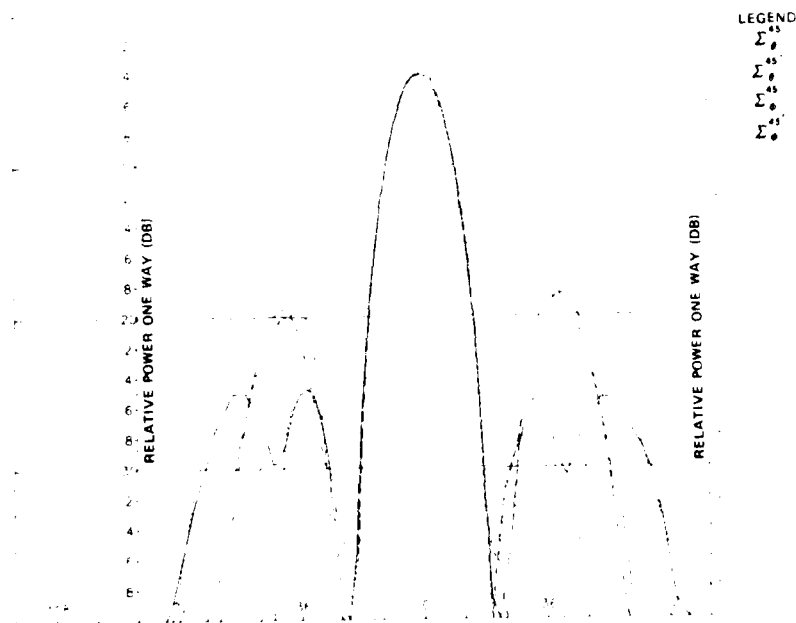
RADOME ANALYSIS EXAMPLE

The motivation for the antenna synthesis procedure described above is to ensure the valid assessment of the accuracies of various computer-aided radome analysis techniques [1], one of which is described in this section.

A computationally fast receiving formulation for radome analysis [9] is illustrated in Figure 11. The antenna near fields \underline{E}_{Ti} , \underline{H}_{Ti} are represented by a uniform grid of sample points on a finite planar aperture surface S_{ap} placed on or just in front of the radiating portion of the actual antenna. The near fields are assumed to be the same as those produced by the antenna when transmitting in the absence of the radome. Rays representing the incident plane wave (target return) are traced from each point in the aperture in the direction \hat{k} to the radome wall. The electromagnetic field associated with each ray is weighted by the insertion



(a) E-Plane Patterns.



(b) Patterns in $\phi = 45^\circ$ Plane.

FIGURE 10. COMPARISONS OF MEASURED AND SYNTHESIZED (1) SUM PATTERNS OF ACTUAL ANTENNA USING 2-D EXTRAPOLATION

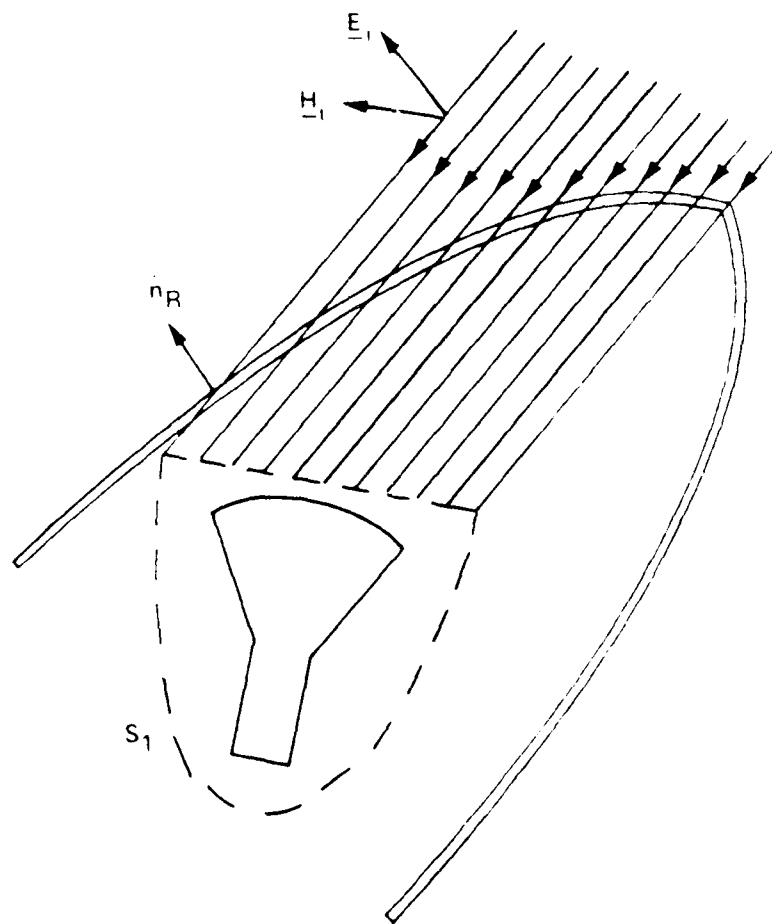


Figure 11. Illustration of the Fast Receiving Method of Radome Analysis

transmission coefficients for field components parallel and perpendicular to the plane of incidence at each point on the radome wall. The response V_R of the antenna is obtained by summing up the contributions of the received fields \underline{E}_R , \underline{H}_R as specified by Lorentz reciprocity; viz.,

$$V_{Ri}(\hat{k}) = C \int_{S_{ap}} (\underline{E}_{Ti} \times \underline{H}_R - \underline{E}_R \times \underline{H}_{Ti}) \cdot \hat{n} \, da \quad (59)$$

The subscript $i=1,2,3$ specifies the antenna near fields for the Δ , Δ_{EL} , and Δ_{AZ} channels, respectively. Antenna patterns can be computed by controlling the direction of arrival and polarization of the incident plane wave. Boresight errors in the two monopulse planes can also be computed for specified antenna/radome orientations by determining the direction of arrival which produces the difference pattern nulls.

The 64×64 sample array of Figure 9(b) representing the near field of the antenna was actually too large to fit into the 10.38λ -diameter, 10.38λ length, tangent ogive, Rexolite ($\epsilon_r=2.54$, $\tan \delta=.002$) radome used in the analysis and measurement. Also, since six such complex arrays are used in the program for the three antenna channels, core memory storage was a consideration. Consequently, only the central 49×49 sample points of the near fields were actually used in the radome computations.

Comparisons of the E-plane Δ_{EL} patterns, measured without the radome and computed using a free space radome, are shown in Figure 12 to demonstrate the adequacy of the synthesis technique and the small effects of the near-field truncation. The pattern in Figure 12 was computed as the response of the antenna to plane waves arriving from 65 directions in the E-plane, equally spaced in $k_y = \sin\theta$ over the visible region $|k_y| \leq 1$. The

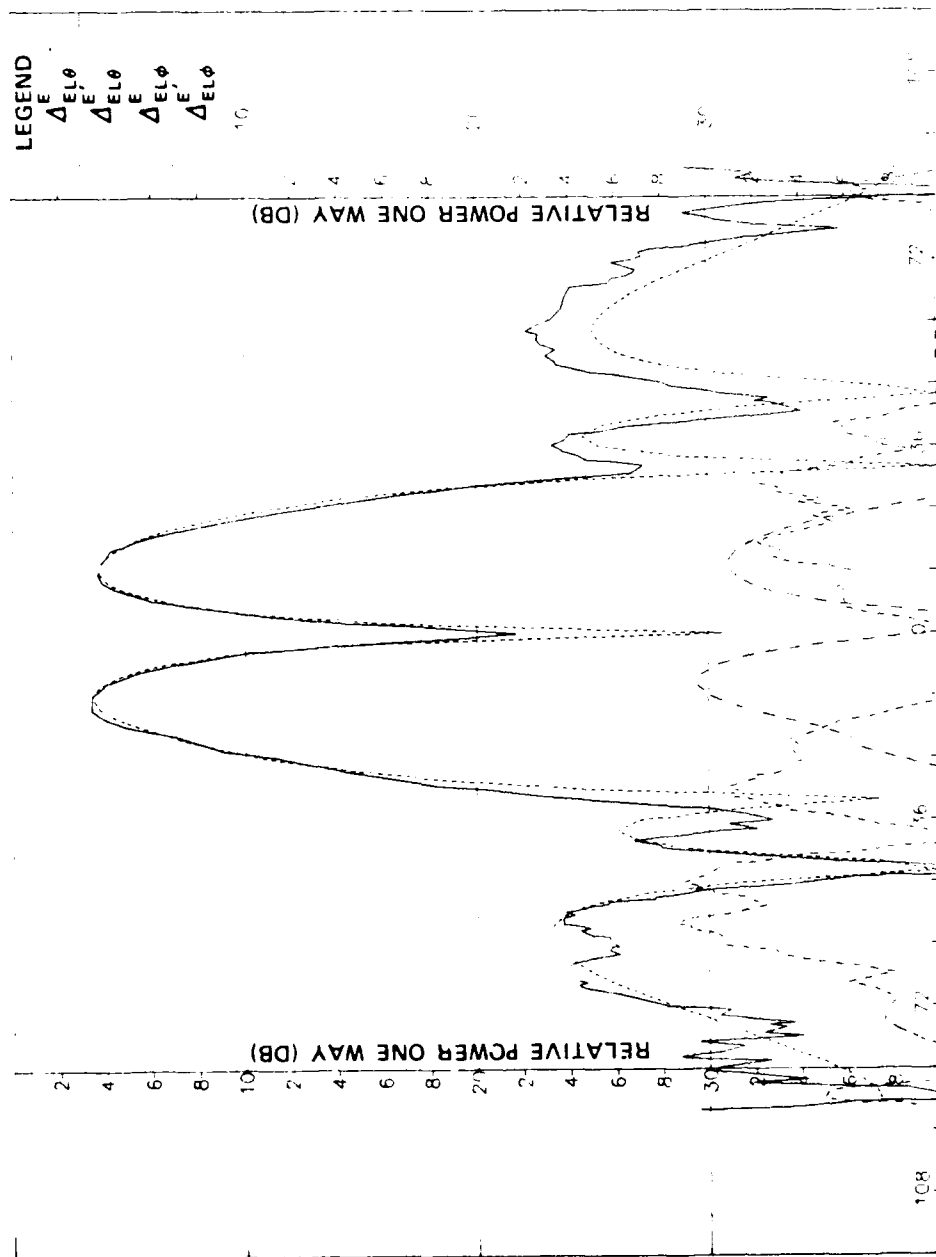


FIGURE 13. COMPARISONS OF MEASURED AND COMPUTED (') E-PLANE DIFFERENCE PATTERNS FOR REXOLITE PADOME.

computed patterns were then Fourier interpolated via Equation (58) to produce sample points at 2° increments over the angular range $|\theta| \leq 90^\circ$.

The computer-aided analysis was repeated using the Rexolite radome, and Δ_{EL}^E E-plane patterns were computed and interpolated as before. The results are graphed in Figure 13 and compared to the measured patterns with the actual radome in place. The radome was oriented with respect to the antenna such that the radome axis of symmetry made an angle of 17° with respect to the antenna z-axis, and the tip of the radome was located in the $\phi = -45^\circ$ plane of the antenna (Figure 2). Agreement is good for the primary Δ_{EL}^E component over the range $|\theta| \leq 36^\circ$; the discrepancies outside this range of angles are attributed to reflections not accounted for in the analysis. The poor agreement between the cross-polarized Δ_{EL}^E components in Figure 13 is attributed to deficiencies in the analysis, particularly the absence of any accounting for reflections inside the radome.

DISCUSSION

It is important to distinguish the band-limited or aperture-limited nature of the plane wave spectra of each element at $z=0$ from the unlimited nature of the PWS of the four-horn array of elements at $z>0$. Each element has finite size; hence, it is a source whose aperture fields have bounded support. It follows that the PWS is not limited in extent in the wavenumber plane since a function and its Fourier transform cannot both have finite support [22]. The unlimited nature of the element plane wave spectra must be taken into consideration when implementing the extrapolation algorithm to minimize the effects of aliasing.

The near field of the four-horn array can be synthesized from the element near field or from its plane wave spectra. The results presented above utilized the latter method, and since no windowing function was applied to the plane wave spectra of the four-horn array, the resulting near fields are theoretically those right at the $z=0$ plane where the elements are located. It is well known that the planar near field changes as a function of z [3]; viz., the plane wave spectrum is modified by the exponential function $e^{-jk_z z}$ so that $E_{nf}(x,y,z) = F(A(k_x, k_y)) e^{-jk_z z}$. For values of z of only a few wavelengths, the effect of the exponential function is to drastically attenuate the evanescent modes of the spectra and to cause the planar near field to spread out. Thus, what was a near field having bounded support at $z=0$ becomes a Fresnel field of unlimited extent with increasing z ; concurrently, the initial spectra having unlimited extent become limited. In the limit of very large z , the spectra have bounded support on the region $\sqrt{k_x^2 + k_y^2} \leq 1$. This interchangeability of the roles of aperture-limited PWS, and wavenumber-limited near fields, is not always fully appreciated.

The synthesis procedure described above also allows for the inclusion of virtually any amount of additional measured pattern data. The additional data form added constraints on the near-field solutions finally obtained in the same way that the principal plane data have worked here.

CONCLUSIONS AND RECOMMENDATIONS

The aperture synthesis procedure described has been demonstrated to yield excellent results, both in terms of the measured versus synthesized patterns and in the reasonableness of the near fields produced. The procedure is specifically applicable to computer-aided radome analysis,

especially in regard to verification of computed results by comparison to measured pattern data.

It is recommended that additional work be carried out to determine the applicability of the method to source synthesis using complete amplitude and phase data, both near-field and far-field. Additional source geometries should be included in the source specification to ensure close conformance with physical fact. It is anticipated that the actual fields of a number of common source geometries can be determined quite accurately from measured radiation data using the general procedure described here.

ACKNOWLEDGMENTS

This research was sponsored by the Air Force Office of Scientific Research under Grant AFOSR-77-3469. The United States Government is authorized to reproduce and distribute reprints for governmental purposes notwithstanding any copyright notation hereon.

The help of Professor R. W. Schafer in defining the extrapolation algorithm is gratefully acknowledged.

REFERENCES

1. G. K. Huddleston, H. L. Bassett, and J. M. Newton, "Parametric Investigation of Radome Analysis Methods," in 1978 IEEE AP-S Symposium Digest, 1978, pp. 199-201.
2. A. C. Ludwig, "Radiation Pattern Synthesis for Circular Aperture Horn Antennas," IEEE Trans., AP-14, No. 4, pp. 434-440, July 1966.
3. P. G. Clemow, The Plane Wave Spectrum Representation of Electromagnetic Fields, Pergamon Press, Oxford, 1966.
4. A. Papoulis, "A New Algorithm in Spectral Analysis and Band-Limited Extrapolation," IEEE Trans., CAS-22, No. 9, pp. 1299-1306, September 1975.
5. G. Tricoles, "Radiation Patterns and Boresight Error of a Microwave Antenna Enclosed in an Axially Symmetric Dielectric Shell," J. Optical Soc. of America, Vol. 54, No. 9, pp. 1094-1101, September 1964.
6. D. T. Paris, "Computer-Aided Radome Analysis," IEEE Trans., AP-18, No. 1, pp. 7-15, January 1970.
7. D.C.F. Wu and R. C. Rudduck, "Application of Plane Wave Spectrum Representation to Radome Analysis," in Proc. of the Tenth Symposium on Electromagnetic Windows, July 1970, pp. 46-49.
8. E. B. Joy and G. K. Huddleston, "Radome Effects on Ground Mapping Radar," Technical Report for U. S. Army Missile Command, AD-778 203, March 1973.
9. G. K. Huddleston, "Radome Analysis Computer Program: Ray Tracing Formulation," Technical Report for Johns Hopkins University Applied Physics Laboratory, November 1979.
10. K. Siawak, T. B. Dowling, and L. R. Lewis, "Boresight Errors Induced by Missile Radomes," IEEE Trans., AP-27, No. 6, pp. 832-841, November 1979.
11. L. G. Bulluck, G. R. Gehl, and J. J. Sparagna, "An Analysis of Wide-Band Microwave Monopulse Direction-Finding Techniques," IEEE Trans., AES-7, No. 1, pp. 188-202, January 1971.
12. J. Arsac, Fourier Transforms and the Theory of Distributions, Prentice-Hall, Inc., Englewood Cliffs, N.J., 1966, Ch. 5.
13. D. E. Rhodes, Synthesis of Planar Antenna Sources, Oxford University Press, London, 1974.

14. H. G. Schmidt-Weinmar, "Spatial Resolution of Subwavelength Sources from Optical Far Zone Data," Chapter 4 of Inverse Source Problems in Optics, H. P. Baltes, editor, Springer-Verlag, Berlin, 1978.
15. G. K. Huddleston, "Optimum Probes for Near-Field Antenna Measurements on a Plane," Ph.D. Dissertation, Georgia Institute of Technology, Atlanta, Georgia, 1978, Ch. 3.
16. S. Silver (ed.), Microwave Antenna Theory and Design, McGraw-Hill, New York, 1949, pp. 161-162.
17. J. D. Kraus, Antennas, McGraw-Hill, New York, 1950, Ch. 15.
18. H. A. Ferwerda, "The Phase Reconstruction Problem for Wave Amplitudes and Coherence Functions," Chapter 2 of Inverse Source Problems in Optics, H. P. Baltes, editor, Springer-Verlag, Berlin, 1978.
19. S. Silver, op. cit., p. 337.
20. Ian N. Sneddon, Fourier Transforms, McGraw-Hill, New York, 1951, Ch. 2.
21. J. W. Goodman, Fourier Optics, McGraw-Hill, New York, 1968, p. 25.
22. H. J. Landau and H. O. Pollak, "Prolate Spheroidal Wave Functions, Fourier Analysis and Uncertainty - I," BSTJ, 40, pp. 43-64, January 1961.

APPENDIX C

"Comparative Accuracies of Radome Analysis Methods"

Accepted for Publication

in

Proceedings of the Fourth International Conference
on Electromagnetic Windows

Toulon, France

June 10-12, 1981

COMPARATIVE ACCURACIES OF RADOME ANALYSIS METHODS

G. K. Huddleston
School of Electrical Engineering
and

H. L. Bassett and M. J. Hadsell
Engineering Experiment Station (RAIL)

Georgia Institute of Technology
Atlanta, Georgia 30332

INTRODUCTION

This paper presents the salient results of a parametric investigation of radome analysis methods [1]. Three methods of analysis were investigated as described below. Measured boresight error data obtained at 35 GHz on eight combinations of three, four-horn monopulse antennas and five polystyrene, tangent ogive radomes are used as true data in assessing the speeds, accuracies, and ranges of validity of the three methods of analysis.

METHODS OF ANALYSIS

Three computer-aided methods of radome analysis were investigated. The theoretical bases for all three methods are the Huygens-Fresnel principle, Lorentz reciprocity, and geometrical optics [2]. The first method, called herein the fast receiving method, uses geometrical optics (ray tracing) to fit the fields incident on the aperture of a monopulse antenna enclosed by the radome due to a TEM wave incident on the radome from a specified direction \hat{k} [3]. The insertion voltage transmission coefficients of flat panel theory for parallel and perpendicular polarization are used to transform the plane wave fields associated with each ray from their values at the incident point on the outside surface of the radome to their values \underline{E}_R , \underline{H}_R at the sample point in the aperture. The voltage received by each channel (Σ , Δ_{EL} , Δ_{AZ}) of the monopulse antenna is obtained according to the reciprocity integral

$$V_{REC}(\hat{k}) = \int_S (\underline{E}_T \times \underline{H}_R - \underline{E}_R \times \underline{H}_T) \cdot \underline{n} \, da \quad (1)$$

where \underline{E}_T , \underline{H}_T are the aperture fields of the antenna when transmitting, and where S is the aperture surface.

The second method of analysis, referred to herein as the fast transmitting method, uses a transmitting formulation based on the plane wave spectrum (PWS) representation of the antenna aperture fields and an equivalent aperture approach [4]. The aperture fields are represented by their samples at MN equally spaced increments in x and y . The two-dimensional Fourier transform of the aperture fields yield the corresponding plane wave spectra. From each sample point, there emanate MN plane waves.

Each plane wave is traced to an incident point on the inner surface of the radome and weighted by the insertion voltage transmission coefficients. The modified fields of each plane wave are then added together at each sample point to produce modified aperture fields which embody the effects of the radome. The voltages received by the radome-enclosed antenna are then calculated according to Equation (1), where \underline{E}_T , \underline{H}_T are the modified aperture fields.

The third method of analysis is referred to as the surface integration method [5]. The voltage received by the antenna enclosed by the radome is again given by Equation (1), where S is now the inside surface of the radome, \underline{E}_T , \underline{H}_T are the radiated fields of the antenna on S , and \underline{E}_R , \underline{H}_R are the fields of the incident plane wave on S as transformed from their values on the outside surface using the insertion voltage transmission coefficients. For some directions of arrival k , portions of the inner radome surface are "shadowed" by other portions; the fields on the shadowed portions are approximated by ray tracing as described above for the fast receiving case. Aperture integration is used to calculate the fields of the antenna at each point on the radome surface from the specified aperture values.

All three methods were implemented in Fortran for execution on the Cyber 70 computing system at Georgia Tech. Maximum use was made of features and software common to all three codes.

ANTENNA/RADOME DESCRIPTIONS

Three, four-horn monopulse antennas were designed and fabricated exclusively for use in this research, corresponding to small ($BW_{3dB}=30^\circ$), medium (15°), and large (8°) sizes. The conical horn elements of each antenna were machined into a single piece of aluminum. The salient dimensions of the antennas are given in Figure 1 and Table 1. More details are given in Reference 6. The elements were y-polarized.

Five, tangent ogive radomes having dimensions given in Figure 1 and Table 2 were machined from cylinders of polystyrene ($\epsilon_r=2.54$, $\tan\delta=.002$), corresponding to small, medium, and large radome sizes. A fineness ratio of 1.0 was used for each size; in addition, for the medium size, fineness ratios of 1.5 and 2.0 were used. All five radomes had a wall thickness of 0.25 inch, corresponding to a full wavelength in the dielectric at 35 GHz and a design angle of approximately 60 degrees.

The antenna and radome were used together in eight different combinations for measurement and analysis purposes. The intent here was to obtain true data from measurements for comparison to the predicted results over ranges of parameters which would help clarify any deficiencies in the three methods of analysis.

RESULTS

Comparisons of measured and computed boresight error data for five antenna/radome combinations are presented in Figures 2 through 5. Bore-sight errors in both the elevation difference channel (BSEEL) and azimuth difference channel (BSEAZ) are shown in each graph as functions of the

radome orientation angle α . The antenna and radome were mounted together such that the radome axis of symmetry passed through the antenna axis of symmetry at the gimbal point (Figure 1b) at an angle of 15 degrees. The radome could then be rotated about the antenna axis of symmetry through the angle α indicated in Figure 1a, thereby placing the tip of the radome in any desired plane of scan. For example, $\alpha=0$ corresponds to the radome tip being in the azimuth plane (+xz-plane) of the monopulse antenna; $\alpha=-90^\circ$ places the tip in the elevation plane (-yz-plane in Figure 1a).

In Figures 2 through 5, α varies from zero to -90 degrees. For $\alpha=0$, symmetry dictates that there should be no boresight error in elevation, and the azimuth boresight error should be nonzero. For $\alpha=-90^\circ$, azimuth boresight error should be zero, and elevation boresight error should be nonzero. The boresight errors are defined here as the true direction to the target in the antenna coordinate system of Figure 1a; e.g., positive boresight error in azimuth (elevation) means that the target lies in the +xz (+yz) plane.

Figure 2 compares the computed results for all three methods with the measured boresight error data. In carrying out the computations for the fast receiving case, it was found that only four points were needed in the antenna aperture, located at the center of each element, to obtain essentially the same results as were computed using a 49×49 point representation of the aperture fields [7]. The same four-point representation was also used in the other two computer codes because the enormous computation times required using the 49×49 point representation were prohibitive. Even using the four-point representation, the surface integration required such long run times that only the small radome could be adequately analyzed on the Cyber system.

Examination of Figure 2 shows that none of the three methods of analysis accurately predicts the measured boresight errors in the case of the small antenna with small radome, especially for the elevation channel. The fast receiving method tends to overestimate the error while the fast transmitting method underestimates it. The surface integration method does the best job for the azimuth error. All three methods predict the correct sign of the error for most of the range of α considered. Deficiencies in the methods of analysis to account for the lack of agreement with measured results cannot be isolated on the basis of the data.

Figures 3 and 4 present results for the medium antenna and medium radomes having two different fineness ratios. The fast receiving method predicts the measured errors most accurately, though not as accurately as desired. The fast transmitting method underestimates the errors. Unstable results were obtained with the surface integration method as indicated in Figure 3, indicating unresolved problems with the computer code. The two fast methods accurately predict the sign of the error, and the fast receiving method does predict accurately an increase in errors with increasing fineness ratio as expected.

Figure 5 presents the results for the medium antenna and large radome. Neither of the two fast methods predicts the elevation error very accurately. Better predicted results are obtained in the azimuth error, with the fast transmitting being more accurate than the fast receiving method.

The computation times and core storage requirements for the three methods of analysis are presented in Table 3 for comparison purposes. For the fast methods of analysis, these two parameters are independent of the radome size, but do depend on the number of points in the antenna aperture: for the fast receiving method, computation time increases directly with the number of points; for the fast transmitting method, the logarithm (base 2) of the computation time increases in the same manner.

The computation time of the surface integration method depends on both the number of points in the aperture and the number of points used to represent the fields on the radome surface. In Figure 2, four points were used for the aperture fields, and 781 points (spaced $\lambda/3$ apart) were used on the radome surface. In Figure 3, 2291 points at $\lambda/3$ spacing were used on the radome surface, and four points were used for the aperture fields.

Comparisons of measured and computed values of on-axis sum channel gain loss relative to the case of no radome are shown in Table 4 for three positions of the radome tip. For the small losses encountered, no method consistently predicted the measured radome losses.

CONCLUSIONS AND RECOMMENDATIONS

The main conclusion to be made from the data presented is that there is room for improvement in the predictive accuracies of the computer codes used with respect to the important parameters of boresight error and radome loss. This conclusion is especially true for the case of small antennas and radomes where the effects of antenna/radome interactions are not properly included. For the case of moderate sized antennas and radomes, the fast receiving method is attractive because of the fast computation time and reasonably accurate results. The surface integration code used requires additional development before any valid conclusions can be drawn about its predictive accuracy; however, it is clear that its applicability will be restricted to small radomes because of the relatively large computation times required.

It is recommended that the fast receiving method be modified so that refractive effects and ray spreading are more accurately accounted for in the ray tracing procedure. It is also recommended that the surface integration method be further developed, even to include first-order reflected fields. Additionally, it is recommended that new experimental techniques be developed which will allow the determination of radome fields close to the dielectric so that deficiencies in the analytical methods can be isolated and corrected.

ACKNOWLEDGMENT

This research was sponsored by the Air Force Office of Scientific Research under grant AFOSR-77-3469. The United State Government is authorized to reproduce and distribute reprints for governmental purposes notwithstanding any copyright notation hereon.

REFERENCES

1. G. K. Huddleston, H. L. Bassett, & J. M. Newton, "Parametric Investigation of Radome Analysis Methods", Annual Report, Grant AFOSR-77-3469, November 1978.
2. G. K. Huddleston, "Theory of Radome Analysis", submitted to IEEE AP-S Transactions, November 1980.
3. G. K. Huddleston, H. L. Bassett, & J. M. Newton, "Parametric Investigation of Radome Analysis Methods: Computed-Aided Analysis Using Geometrical Optics and Lorentz Reciprocity", Final Technical Report, Vol. 2 of 4, Grant AFOSR-77-3469, February 1981.
4. E. B. Joy & G. K. Huddleston, "Radome Effects on the Performance of Ground Mapping Radar", Final Technical Report, U. S. Army Missile Command, DAAH01-72-C-0598, March 1972.
5. G. K. Huddleston, H. L. Bassett, & J. M. Newton, "Parametric Investigation of Radome Analysis Methods: Computer-Aided Radome Analysis Using the Huygens-Fresnel Principle and Lorentz Reciprocity", Final Technical Report, Vol. 3 of 4, Grant AFOSR-77-3469, February 1981.
6. H. L. Bassett, J. M. Newton, et al., "Parametric Investigation of Radome Analysis Methods: Experimental Results", Final Technical Report, Vol. 4 of 4, Grant AFOSR-77-3469, February 1981.
7. G. K. Huddleston, "Aperture Synthesis of Monopulse Antenna for Radome Analysis Using Limited Measured Pattern Data", Proceedings Southeast-con '81, April 1981.

Table 1. Dimensions in Inches of Antennas. (See Figure 1(a)).

<u>Antenna Identification</u>	<u>R_A</u>	<u>Element Diameter A</u>	<u>Element Half- Spacing C</u>	<u>Overall Diameter B</u>
Small	.1875	.310	.160	.875
Medium	.250	.620	.320	1.540
Large	.375	1.225	.878	3.040

Table 2. Dimensions in Inches of Radomes. (See Figure 1(b)).

<u>Radome Identification</u>	<u>Outside Diameter D</u>	<u>Outside Length C</u>	<u>Inside Diameter E</u>	<u>Inside Length B</u>	<u>R_R</u>
Small (F=1.0)	2.55	2.35	2.05	2.05	.4375
Medium (F=1.0)	4.00	3.81	3.50	3.50	.75
Medium (F=1.5)	4.00	5.66	3.50	5.25	.75
Medium (F=2.0)	4.00	7.52	3.50	7.00	.75
Large (F=1.0)	6.91	6.72	6.41	6.41	.375

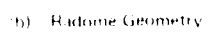
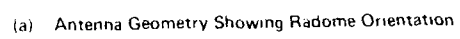
Table 3. Computation Time and Core Storage Requirements.

<u>Case</u>	Computation Time*(sec.)/Core Storage (octal)		
	<u>Fast Receiving</u>	<u>Fast Transmitting</u>	<u>Surface Integration</u>
Small Antenna, Small Radome	.24/67100	.62/77300	34.0/135300
Medium Antenna, Medium (F=1.0)	.25/67100	.62/77300	44.0/135300

*Per look angle.

Table 4. Radome Loss Comparisons.

<u>Antenna</u>	<u>Radome</u>	Loss (dB)				
		<u>Alpha (Deg.)</u>	<u>Measured</u>	<u>Fast Revg</u>	<u>Fast Xmtg</u>	<u>Surface Integration</u>
Small	Small	0	0.4	0.5	0.5	1.9
"	"	-45	0.7	0.5	0.4	1.7
"	"	-90	0.6	0.3	0.3	1.9
Medium	Medium (F=1.0)	0	1.4	0.4	0.6	1.2
"	" "	-45	1.4	0.4	0.5	1.2
"	" "	-90	0.8	0.3	0.4	1.2
Medium	Medium (F=2.0)	0	0.2	0.1	0.6	-
"	" "	-45	0.5	0.1	0.4	-
"	" "	-90	0.6	0.1	0.2	-



10

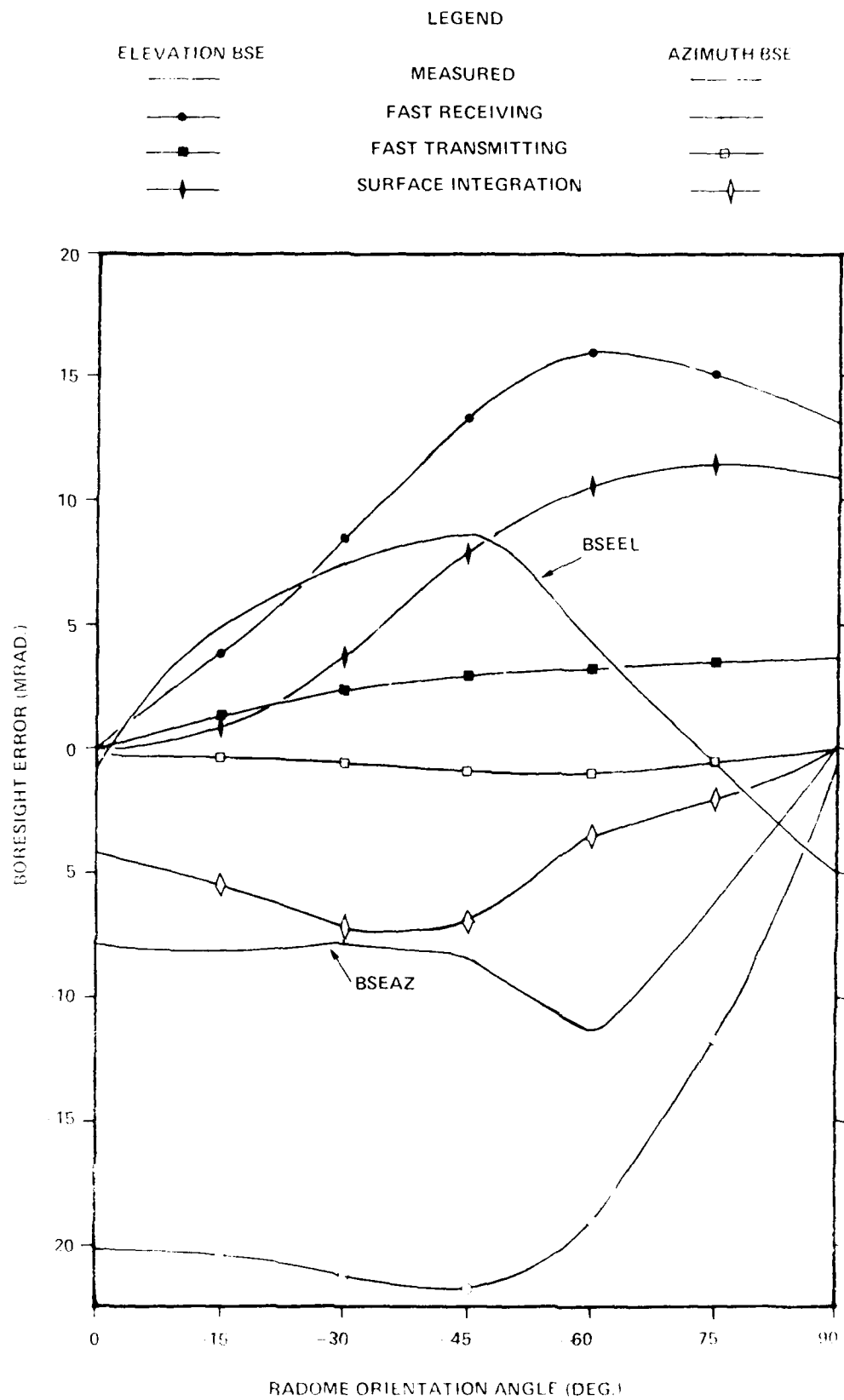


Figure 2. Comparisons of Measured and Computed Boresight Errors for Small Antenna, Small ($F = 1.0$) Radome.

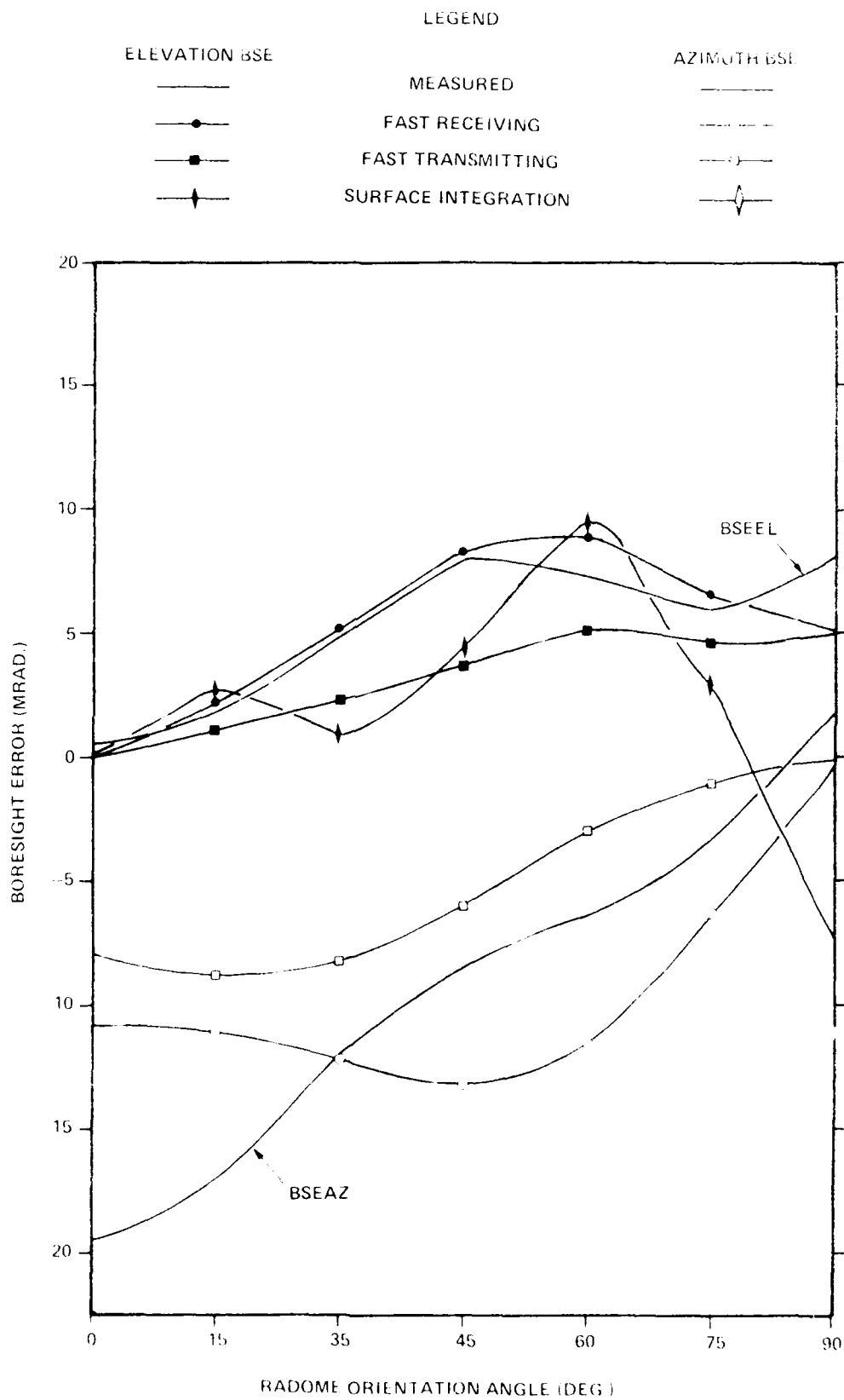


Figure 3. Comparisons of Measured and Computed Bore-sight Errors for Medium Antenna, Medium ($F = 1.0$) Radome.

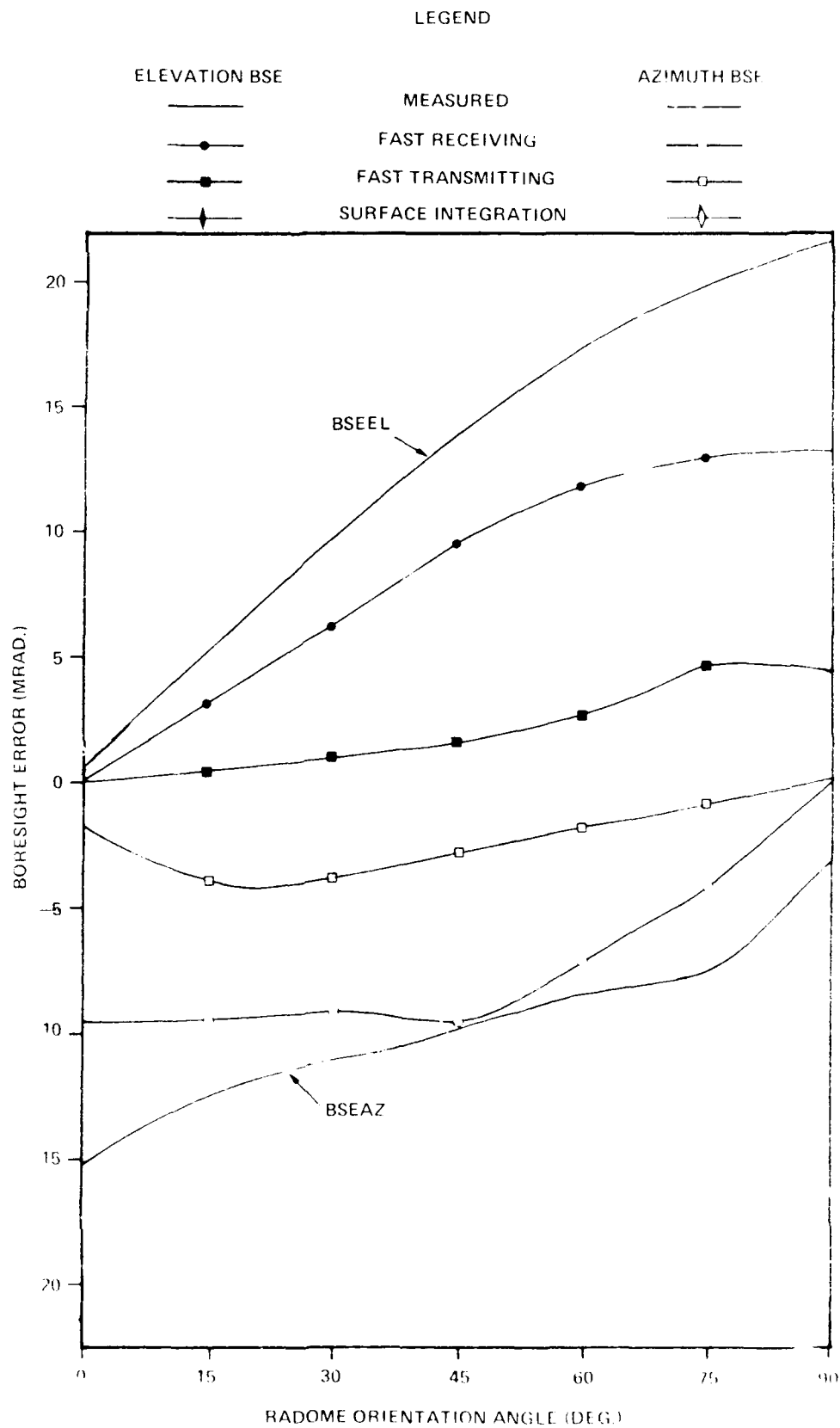


Figure 4. Comparisons of Measured and Computed Boresight Errors for Medium Antenna Medium (F = 2.0) Radome

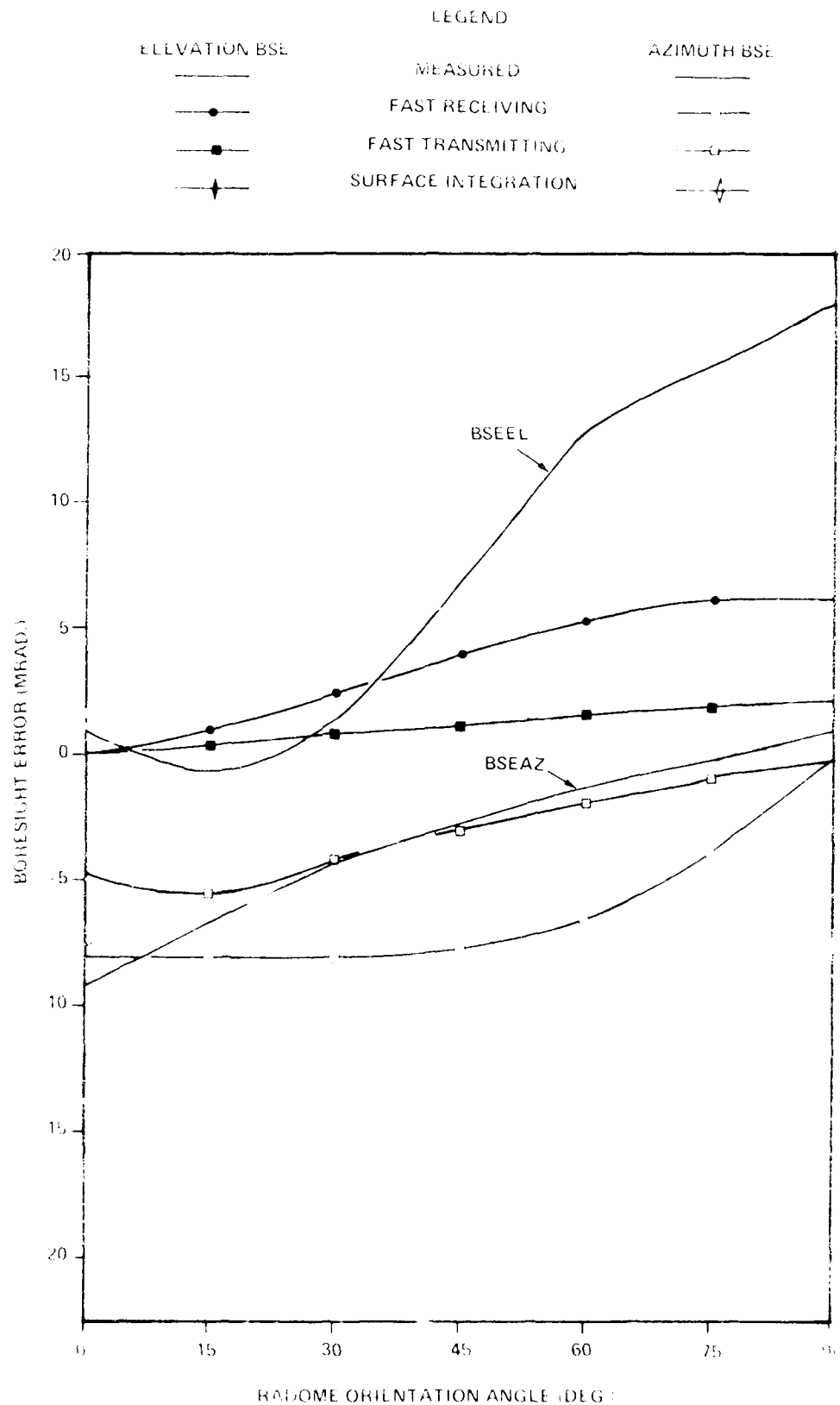


Figure 3: Comparisons of Measured and Computed Boresight Errors for Medium Antenna, Large ($\epsilon = 1.0$) Radome